International Journal of Earth Sciences (2024) 113:501–521
https://doi.org/10.1007/s00531-024-02390-1

ORIGINAL PAPER

Age, origin and tectonic controls on rapid recent exhumation of the Sibela Mountains, Bacan, Indonesia

Juliane Hennig-Breitfeld[1,2] · Robert Hall[2] · Lloyd T. White[3] · H. Tim Breitfeld[1,2] · Marnie A. Forster[4] · Richard A. Armstrong[4] · Barry P. Kohn[5]

Received: 5 December 2023 / Accepted: 20 January 2024 / Published online: 8 March 2024

Abstract

The Sibela Mountains of the island of Bacan in eastern Indonesia contain one of the Earth's youngest metamorphic complexes that is now exposed at elevations up to 2000 m. New mica $^{40}Ar/^{39}Ar$ and apatite (U–Th–Sm)/He data from metamorphic and igneous rocks indicate that these rocks were rapidly exhumed in the Pleistocene (c. 0.7 Ma). Exhumation of the metamorphosed Permo-Triassic basement (c. 249–257 Ma) was accompanied by metamorphism (recorded by schists) as well as partial melting (recorded by c. 1.4 Ma granitic dykes). These processes must have occurred at extremely high cooling and exhumation rates. The rapid exhumation on land was associated with significant subsidence in adjacent basins offshore that reach depths up to 2.4 km. Neogene metamorphic core complexes and other metamorphic complexes are well-known from eastern Indonesia, but they usually record much higher exhumation rates than those reported from older classic metamorphic core complexes found in other parts of the world and require a different formation mechanism. Unlike classic metamorphic core complexes that are characterized by low-angle detachment faults, the Bacan metamorphic rocks were exhumed on steep bounding normal faults forming a rectilinear block pattern. We suggest such complexes are termed metamorphic block complexes (MBC). The Bacan MBC is exceptionally young and like the other east Indonesian complexes was rapidly exhumed during subduction rollback. A flexure formed during arc-arc collision as the Sangihe forearc loaded the Halmahera forearc which reactivated steeply-dipping faults in a rectilinear chocolate block pattern.

Keywords Bacan · Metamorphic block complex · Subduction rollback · U–Pb zircon geochronology · $^{40}Ar/^{39}Ar$ thermochronology · (U–Th–Sm)/He thermochronology

Introduction

SE Asia is one of the most tectonically active regions in the world, where the Indian-Australian, Eurasian, Philippine Sea and Pacific plates converge. The island of Bacan is situated in the North Moluccas, in an area partly bounded by the Halmahera Thrust to the west and the Sorong Fault Zone to the south which runs from the Bird's Head Peninsula of New Guinea in the east towards the island of Sulawesi (Fig. 1a). Bacan is situated at the southern end of the Halmahera oceanic volcanic arc where geochemical studies of volcanic rocks indicate the arc intersects a continental crustal fragment at depth below Bacan (Morris et al. 1983). Central Bacan includes an exposed area of high-grade continental metamorphic rocks in the Sibela Mountains from sea level to elevations of more than c. 2000 m which are the highest in the North Moluccas (Fig. 1b). The history of the metamorphic rocks is uncertain; they have not been dated but have been assumed to be Paleozoic or older and have

✉ H. Tim Breitfeld
tim.breitfeld1@geo.tu-freiberg.de

1 Institute of Geology, TU Bergakademie Freiberg, Bernhard-von-Cotta-Straße 2, 09599 Freiberg, Germany

2 SE Asia Research Group, Department of Earth Sciences, Royal Holloway University of London, Egham, Surrey TW20 0EX, UK

3 GeoQuEST Research Centre, School of Earth, Atmospheric and Life Sciences, University of Wollongong, Wollongong, NSW 2522, Australia

4 Research School of Earth Sciences, Australian National University, Canberra, ACT 0200, Australia

5 School of Geography, Earth and Atmospheric Sciences, University of Melbourne, Melbourne, VIC 3010, Australia

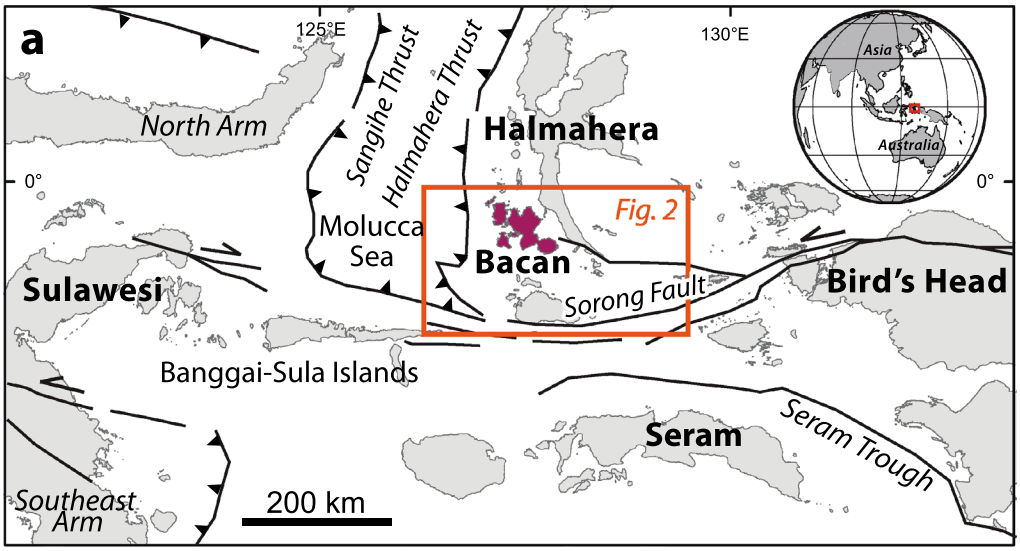

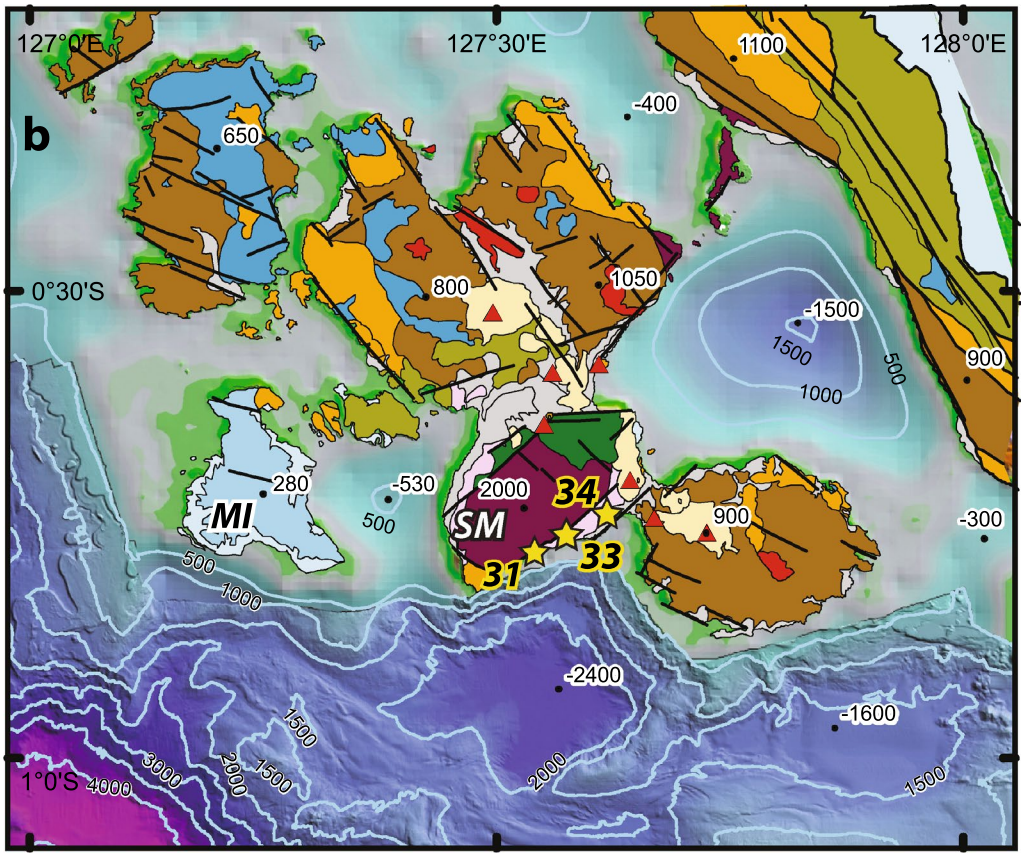

Quaternary volcanoes
Alluvium
Alluvial fan
Quaternary limestone
Quaternary volcanic
Mio-Pliocene limestone
Mio-Pliocene volcanic/ volcaniclastic
Miocene limestone
Miocene clastic
Granite
Paleogene volcanic/ volcaniclastic
Ophiolite
Metamorphic

◂**Fig. 1** The study area on Bacan island, eastern Indonesia. **a** Bacan is situated southwest of Halmahera north of the Sorong Fault Zone and east of the Halmahera Thrust (Silver and Moore 1978). **b** Geological map of Bacan based on Malaihollo and Hall (1996), including sample locations (yellow stars). The area comprises highly elevated regions and deeply subsided basins (elevations in m above and below sea level). *SM* Sibela Mountains, *MI* Mandioli island

an Australian origin (Brouwer 1921; Hamilton 1979; Hall et al. 1988).

The age, exhumation mechanism and rate and are unknown for the metamorphic rocks in the Sibela Mountains. Steep incised valleys at the mountain edges, uplifted young coral reefs and high topography suggest very young and rapid uplift. Basins with depths as great as 2.4 km surrounding the island of Bacan suggest contemporaneous subsidence. Rapidly exhumed metamorphic complexes in SE Asia have been identified elsewhere in east Indonesia and Papua New Guinea. Some of these have been described as metamorphic core complexes, for example, those in north and central Sulawesi (van Leeuwen and Muhardjo 2005; Spencer 2011), West Papua (White et al. 2019) and Papua New Guinea (Little et al. 2007). Other metamorphic complexes in Seram and northwest Sulawesi have been described as exhumed in a core complex-style (Pownall et al. 2014) or as similar to core complexes but lacking a main detachment fault (Hennig et al. 2017), with cooling rates (Pownall et al. 2014, 2017a; Hennig et al. 2017) that exceed those typically reported for classic metamorphic core complexes (65–280 °C/Ma, e.g. Scott et al. 1998; Vanderhaeghe et al. 2003; Whitney et al. 2013).

The metamorphic rocks exposed in the Sibela Mountains in Bacan lack a clearly identifiable detachment fault and are unlikely to represent a classic metamorphic core complex. Here we report new field observations, as well as new geochronological and thermochronological data obtained from the metamorphic complex in the Sibela Mountains on Bacan (Fig. 1b), which enable assessment of its young Neogene-Quaternary evolution and record rapid exhumation associated with steeply dipping faults. This requires a formation mechanism different from that of classic metamorphic core complexes, as discussed below.

Geological background

Bacan is the largest island west of Halmahera at the southern end of the Halmahera arc. It is known to be underlain by continental crust, at least in part, based on geochemical studies of volcanic rocks (Morris et al. 1983; Forde 1997) and observations of metamorphic rocks on the island (Brouwer 1921; Hamilton 1979). Metamorphic rocks of different grades form the Sibela Mountains on Bacan (Brouwer 1921; Hamilton 1979; Yasin 1980; Hall et al. 1988; Malaihollo and Hall 1996). The Sibela Continental Suite forms the southern part of the Sibela Mountains (Fig. 1b) and includes schists and gneisses of upper amphibolite facies containing garnet, kyanite and staurolite (Brouwer 1921); all record multiple phases of deformation (Malaihollo and Hall 1996). These metamorphic rocks were undated before this study; Hamilton (1979) proposed they were Paleozoic, and Malaihollo and Hall (1996) suggested they included Precambrian continental crust derived from Australia.

Apart from the Sibela continental metamorphic rocks, the basement exposed in Bacan includes the Sibela ophiolite, a Cretaceous arc-related incomplete ophiolitic complex (Hall et al. 1988; Malaihollo and Hall 1996) in the northern part of the Sibela Mountains, and Eocene to Lower Miocene volcanic and volcaniclastic rocks in the northern and southern parts of the island (Fig. 1b). The basement rocks are intruded by Neogene granitoids and diorites, and unconformably overlain by Lower to Middle Miocene shallow marine limestones interbedded with clastic sediments, and Upper Miocene to Pliocene volcanic rocks, volcaniclastics, and limestones deposited in a nearshore shallow-marine environment (Malaihollo and Hall 1996). The youngest shallow marine sedimentary rocks dated using foraminifera (Hall et al. 1992) have a middle to late Pliocene age.

Based on geological mapping Yasin (1980) interpreted the Sibela Mountains as a horst block and identified active faults with trends of NW–SE and NE–SW, some marked by hot springs. Silitonga et al. (1981) also identified N–S and E–W fault trends and interpreted Bacan as broken into fault-bounded horst and graben blocks. They divided Bacan into three parts based on its topography. The central part is a 2 km high horst block (Fig. 1b) of crystalline schists and basic and ultrabasic rocks. This is separated by a narrow swampy depression trending NE-SW, interpreted as a graben, from the northern part of the island which reaches heights of 1 km (Fig. 2) and has a basement of mainly Paleogene intermediate volcanic rocks and phyllites. The northern part of the island is split by a NW–SE graben-like depression (Fig. 2). A narrow NE-SW trending depression on the SE side of the Sibela Mountains is another graben that separates the central block from the third part of the island (Fig. 2) which also has a basement of Paleogene intermediate volcanic rocks and reaches heights of almost 1 km (Fig. 1b). Silitonga et al. (1981) observed that lineaments interpreted from air photos in coastal regions indicate recent movements around the margins of the island. They reported that the boundary fractures of the Sibela horst have acted as channels for recent basaltic eruptions.

The Cenozoic tectonic history of Bacan is complex and includes several phases of contraction and extension. Cretaceous to Paleogene Philippine Sea plate rocks were thrust over the Australian continental crust in Halmahera during the arc-continent collision in the Early Miocene

(Hamilton 1979; Moore and Silver 1983; Hall 1987; Hall et al. 1988). Australian continental crust was emplaced below Bacan during this collision. The Sibela Mountains expose continental crust and parts of the Cretaceous arc (Hall et al. 1988; Malaihollo and Hall 1996). After the collision shallow marine carbonates were deposited throughout the Halmahera and Bacan region during the Early to Middle Miocene. Eastward subduction of the Molucca Sea started in the Middle Miocene, contemporaneous with westward subduction beneath the Sangihe arc, to form the well-known double subduction system and resulted in arc magmatism on Bacan (Baker and Malaihollo 1996; Forde 1997; Hall 2012) which continued during the Quaternary (Morris et al. 1983) and has now almost ceased. Collision of the Halmahera and Sangihe arcs began at c. 2 Ma (Hall 2000; Hall and Smyth 2008; Hall and Spakman 2015) and convergence of the two forearcs formed the central Molucca Sea collision complex. The collision complex is bounded to the southeast by the Sorong strike-slip fault.

Methodology

New field observations and remote sensing

Our mapping and sampling were undertaken during five field expeditions between 1984 and 2010. Structural observations were acquired during fieldwork, initially using air photos for location, but during expeditions in the 1990s and more recently used Shuttle Radar Topography Mission (SRTM) imagery (Farr and Kobrick 2000) with GPS locations. Offshore, detailed mapping is based on high-resolution multibeam bathymetry with a pixel size of 15–25 m (Orange et al. 2010), so it is possible to map faults and other features offshore with a similar resolution to that using SRTM topography on land. Figure 2 shows land topography and offshore bathymetry based on SRTM elevation data on land, combined with multibeam bathymetry in the southern part of the map. North of approximately 0° 30'S the map has less detail offshore and is based on 30 arc seconds global bathymetry (Becker et al. 2009).

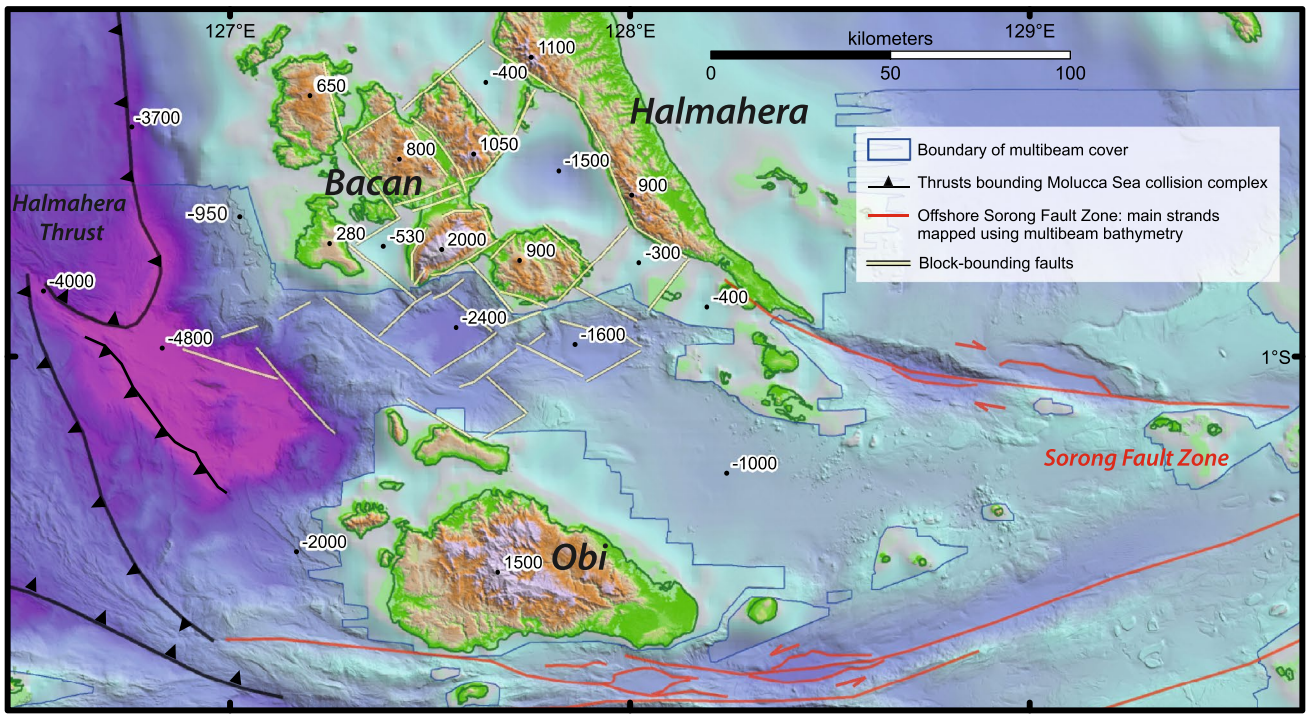

Fig. 2 Bacan and the surrounding area are characterized by a rectilinear fault pattern which separates highly elevated regions from deeply subsided basins. In contrast, the western fault strands of the Sorong Fault Zone to the east and south of Bacan are marked by elongate strike-slip basin geometries. Fault analysis is based on field observations on Bacan, air photos and remote sensing from high resolution 30 m Shuttle Radar Topography Mission (SRTM) imagery on land (Farr and Kobrick 2000), 15–25 m multibeam bathymetry offshore within the area outlined by blue line and 30 arc second global bathymetry (Becker et al. 2009) for the offshore region without multibeam bathymetry

Sample selection

Two staurolite-garnet schists (31H, 34B), one biotite schist (31E), three gneisses (31B, 31G-D, 33B), and one cross-cutting granite dyke (31G-L) were collected from cobbles and boulders of an alluvial fan conglomerate at sample sites 31, 33, and 34 at the foot of the southeastern flank of the Sibela Mountains (Fig. 1b; Table 1). The alluvial fan rocks form a band trending NE-SW, up to a few hundred meters wide, and were deposited against a steep faulted slope that rises rapidly a short distance inland from the sea (Fig. 3a-c). Boulders are typically about 1 m across (Fig. 3d) although a few reach 2 m. The metamorphic rocks on the NW side of the fault are almost inaccessible because of the steepness of the slope and dense rainforest. Narrow valleys incise the upper parts of the alluvial fan before the metamorphic rocks are reached down which large waterfalls flow. To the NE metamorphic rocks are exposed in outcrop at the coast and are light-colored granite gneisses and dark staurolite-garnet schists, identical to boulders sampled in the alluvial fan further SW. The metamorphic rocks were investigated on the NW side of the Sibela Mountains in 1984 (Hall et al. 1988) where the faulted surface between the alluvial fan and the metamorphic rocks to the SE is slightly less steep and it was possible to follow the fast-flowing streams upslope, passing round waterfalls, aided by roots and trees, to about 900 m elevation, above which access was effectively impossible. Again, the rocks found in the outcrop are identical to the boulders found in the alluvial fan and are dominated by garnet-mica schists, staurolite-garnet schists and quartzo-feldspathic gneisses. This indicates that the sampled boulders were derived from nearby outcrops and offer the possibility to study the inaccessible in-situ basement from boulders.

Isotopic analyses

Isotopic analysis and age dating were conducted on selected minerals separated from the seven samples described in the previous section and listed in Table 1. Full analytical data and $^{40}Ar/^{39}Ar$ analysis specification parameters are provided in supplements 1.1–1.5. Biotite-gneiss samples 31B and 31G-D, calc-silicate gneiss 33B and the cross-cutting dyke 31G-L were analyzed by zircon U–Pb geochronology. 31G-D and 31G-L were also analyzed with apatite (U–Th–Sm)/He thermochronology to constrain their uplift history. Schistose samples 31H, 34B and 31E were analyzed by mica $^{40}Ar/^{39}Ar$ thermochronology to investigate the cooling history of the metamorphic rocks.

Zircon U–Pb ages and oxygen isotopes

Zircon grains were separated at Royal Holloway University of London using standard heavy mineral funnel separation procedures (e.g. Mange and Maurer 1992). The samples were crushed in a jaw crusher and rock chips were washed using nylon tissue meshes to obtain a grain size fraction of 63–250 µm. The magnetic fraction was extracted using a hand magnet and the remaining fraction was run through sodium polytungstate (SPT) heavy-density liquid (density of ~ 2.9 g/ cm^3), rinsed with distilled water, and dried in an oven at 40 °C. Zircons were separated from the heavy mineral fraction by using a Frantz magnetic barrier separator (1.7 A, 20° tilt angle), di-iodomethane (DIM) heavy-density liquid (~ 3.3 g/cm^3) and hand-picking techniques.

The mounted zircons were analyzed with SHRIMP-II (U–Pb) and SHRIMP-SI ($^{18}O/^{16}O$) at the Australian National University. These analyses were referenced to the TEMORA 2 U–Pb age and oxygen standard (416.8 ± 1.0 Ma; Black et al. 2004) and SL13 uranium concentration standard (Claoué-Long et al. 1995). Data reduction followed the method described by Williams (1997). Analytical data is listed in Supplements 1.1 and 1.2. Photomicrographs were taken in reflected and transmitted light to detect cracks and inclusions and cathodoluminescence (CL) imaging was carried out on a JEOL JSM 6610A scanning electron microscope to detect internal features of the zircons (i.e., growth zonation, core-rim sites). The beam size varied from 10 to 20 µm for rim and core analyses, respectively. Cathodoluminescence images of analysed zircons can be found in Supplement 2.

Ages greater than c. 100 Ma were corrected for common Pb using measured ^{204}Pb. Cenozoic ages are ^{207}Pb common lead-corrected ^{206}Pb-^{238}U ages assuming a $^{206}Pb/^{238}U$-$^{208}Pb/^{235}U$ age-concordance, because of the

Table 1 List of samples analyzed in this study with locations and analytical methods

Sample ID	Latitude	Longitude	Lihtology	U–Pb	$^{40}Ar/^{39}Ar$	(U–Th–Sm)/He
31H	– 0.793754	127.527032	Staurolite-garnet schist		White mica	
34B	– 0.753426	127.619291	Staurolite-garnet schist		White mica	
31E	– 0.793754	127.527032	Biotite schist		Biotite	
31B	– 0.793754	127.527032	Biotite-gneiss	Zircon		
31G-D	– 0.793754	127.527032	Biotite-gneiss	Zircon		Apatite
31G-L	– 0.793754	127.527032	Granite dyke	Zircon		Apatite
33B	– 0.771370	127.570608	Calc-silicate gneiss	Zircon		

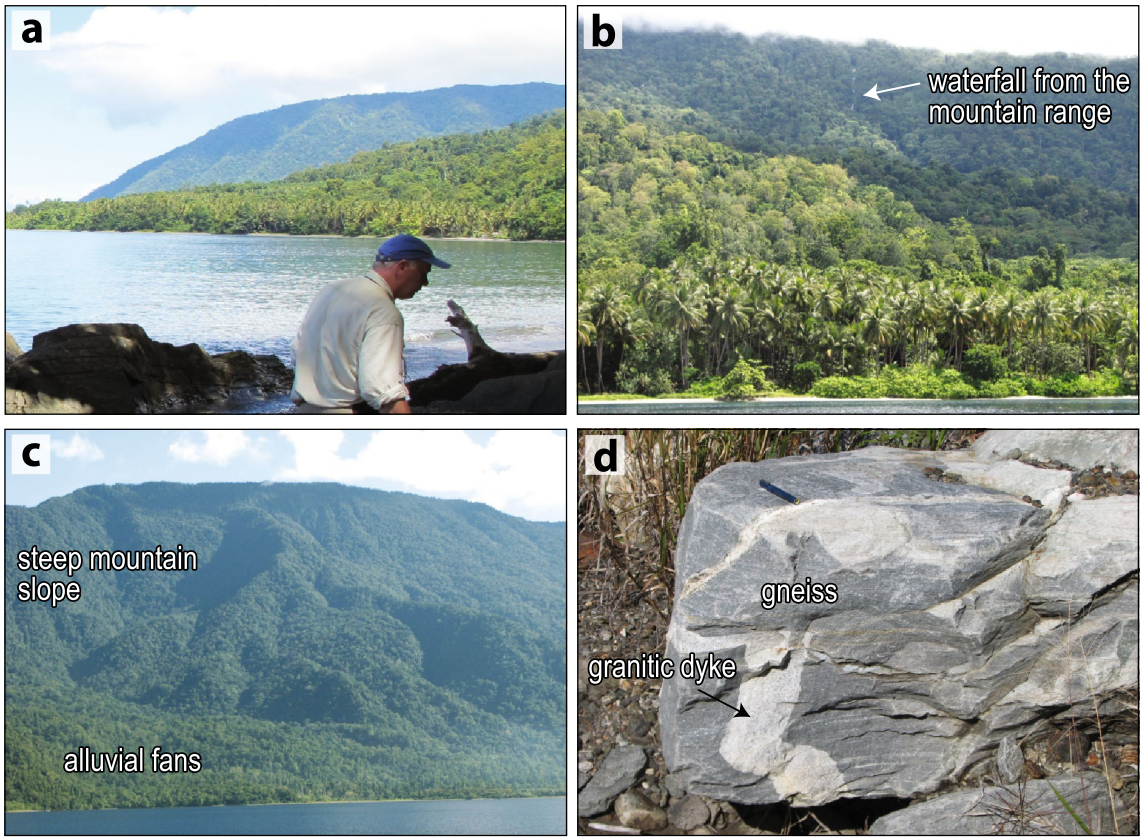

Fig. 3 Field photographs of the Sibela Mountains in southern Bacan. **a**–**c** The thickly forested mountain range has steep and deeply incised slopes and reaches 2 km elevation. Large alluvial fans at the foot of the mountains are covered by rainforest and palm plantations but show distinctive gentle slopes. **d** The alluvial fan breccio-conglomerates contain large boulders of metamorphic rocks intruded by multiple generations of granite dykes

low concentration of ^{204}Pb, ^{207}Pb and ^{208}Pb. This assumes each analysis is a mixture of common and radiogenic lead and subsequently unmixed from the measured ^{207}Pb-^{208}Pb ratio (e.g. Muir et al. 1996). An independent age estimate from the ^{207}Pb-^{206}Pb ratio cannot be determined, so the age is determined from the ^{238}U-^{206}Pb ratio (Muir et al. 1996). Ages greater than 1000 Ma are calculated from ^{207}Pb/^{206}Pb ratios and ages less than 1000 Ma are calculated from ^{206}Pb/^{238}U ratios, as these yield more reliable results because of uncertainties in common Pb corrections. All errors quoted in the text are at the 1σ level. Isoplot 4.11 (Ludwig 2012) was used to display the data on conventional Concordia diagrams (Wetherill 1956) for samples with ages of Permo-Triassic and older, and Tera-Wasserburg Concordia diagram (Tera and Wasserburg 1972) for the Pleistocene dyke. These were used to visually assess outliers (e.g. lead loss, common lead and inheritance). Any outliers were eliminated prior to the calculation of the weighted mean age.

Mica ^{40}Ar/^{39}Ar

Micas were separated using a Frantz electromagnetic separator and purified by hand-picking. Separates were irradiated at the UC Davis McClellan Nuclear Radiation Centre in California, USA with the GA1550 standard (98.5 ± 0.8 Ma; Spell and McDougall 2003) using methodology described by Forster and Lister (2004, 2014), and analyzed at the Research School of Earth Sciences, ANU, Canberra, including incremental heating in a double-vacuum resistance furnace. Analysis was conducted on an ARGUS VI Multi-collector Mass Spectrometer, with data reduction using the software Noble v1.8 and *eArgon* (Supplements 1.3 and 1.4) following the approach by Forster and Lister (2004) and Beltrando et al. (2009). Separates were analyzed with 30 steps and with temperatures rising from 450 to 1450 °C (Lovera et al. 1989). The data reported have been corrected for system backgrounds, mass discrimination, fluence gradients and atmospheric contamination. Errors associated with the age determinations are one-sigma uncertainties and exclude errors in the age of the standard GA1550. Decay constants are those of Steiger and Jager (1977). The ^{40}Ar/^{39}Ar dating

technique is described in detail by McDougall and Harrison (1999) and Forster and Lister (2009).

Apatite (U–Th–Sm)/He

Apatites from samples 31G-L and 31G-D (Supplement 1.5) were extracted using standard heavy mineral separation procedures after Mange and Maurer (1992). Suitable crystals were analyzed at the University of Melbourne, using a solid-state diode laser for helium extraction coupled to a Balzers quadrupole mass spectrometer after the analytical approach of Gleadow et al. (2015) and referenced to analyses of Durango fluorapatite (31.02 ± 1.01 Ma; McDowell et al. 2005). A triplicate single-grain analysis was usually performed unless the helium gas concentration was too low, in which case four to seven grains were combined in one analysis. The grain parameters, including length, radius, morphology, alpha-ejection correction, and effective U concentration (eU), as well as the number of grains per analysis and the age results, are listed in Supplement 1.5.

Results

Remote sensing and field observations

Faulting on land and Sibela Mountains uplift

Structural interpretation supports the rectilinear pattern of NE–SW and NW–SE faults identified by Yasin (1980) and Silitonga et al. (1981). Direct observation of faults is made difficult by thick rainforest vegetation cover and steep terrain (Fig. 3a–c), and air photo interpretation is incomplete in some areas due to cloud cover. However, faults can be mapped on land from air photographs and SRTM imagery which show they have straight traces, indicating a steep dip (Fig. 2; Supplement 3a, b). The faults bound the elevated blocks, such as the Sibela Mountains, which are separated by commonly swampy graben. The Sibela Mountains block exceeds 2 km in elevation.

At the edges of the Sibela Mountains there are clear changes from steep mountain slopes with deeply incised valleys to large alluvial fans dominated by breccio-conglomerates at the coast and at the foot of the mountains (Fig. 3a–c). None of the underlying shallow marine Upper Miocene to Pliocene clastic sediments in the northern and southern parts of Bacan or the surrounding smaller islands contain metamorphic rock clasts or grains. Their sedimentary structures typically indicate predominantly shallow and low-energy depositional environments. Some sediments contain pyroclastic horizons and evidence of rapid deposition, such as dewatering structures and slumps, and storm horizons, indicating contemporaneous volcanic activity but contain no evidence of metamorphic sources.

The alluvial fans deposited at the flanks of the Sibela Mountains (Fig. 3c), especially on the NW and SE sides, contain boulders of coarse-grained high-grade schists, granites and granite gneisses (Fig. 3d). Since no metamorphic material is found in the youngest Pliocene marine sediments we interpret this to indicate uplift began in the Late Pliocene or later and the coarse alluvial fan breccio-conglomerates are Late Pliocene to Quaternary. Late Pliocene or younger uplift of the Sibela block is indicated by Quaternary coral reef limestones now at a height of 700 m on Buku Genem (Mollat 1979, in Silitonga et al. 1981) in the NE part of the Sibela Mountains (Fig. 4). Today, Quaternary reefs fringe the northeast end of the Sibela Mountains and Mandioli island to the west of the Sibela Mountains (Fig. 4). Several boiling hot springs emerge in the sea close to the faults on the SE side of the Sibela Mountains, indicating present-day tectonic activity. The location of Neogene intrusive igneous rocks and Quaternary basic volcanic rocks (Fig. 1b) in both the northern and southern parts of Bacan are linked to the NW–SE and NE–SW steep faults (Yasin 1980; Silitonga et al. 1981; Baker and Malaihollo 1996; Malaihollo and Hall 1996) indicating the faults have influenced the locations of magmatism from at least the Early Miocene until the Quaternary. Continuing uplift is suggested by colonial forts in the Bacan islands dating from the late sixteenth century, originally constructed close to the coast and now situated some distance inland.

Faulting offshore and basins around Bacan

The rectilinear pattern of faulting observed on land can also be observed offshore around Bacan based mainly on high-resolution multibeam bathymetry (Figs. 2 and 4). The mapping offshore shows a similar pattern to that on land with major steep faults trending NE-SW and NW–SE outlining numerous rectilinear blocks of approximately 10–20 km width (Fig. 4). Most of the offshore lineaments are sharply defined indicating they are active features with little sedimentary cover. Blocks on land, such as those of northern and southern Bacan reach elevations up to 1 km and in the Sibela Mountains elevations of more than 2 km. Offshore the basin south of the Sibela Mountains is approximately 2.4 km deep and that south of southern Bacan is around 1.6 km deep (Fig. 1b). The basin northeast of the Sibela Mountains is approximately 1.5 km deep based on the global 30-arc seconds bathymetry, and intermittent records of depths from depth sounder instruments used on boats during fieldwork in the region.

On the SE side of the Sibela Mountains closely spaced topographic contours characterize the northwestern side

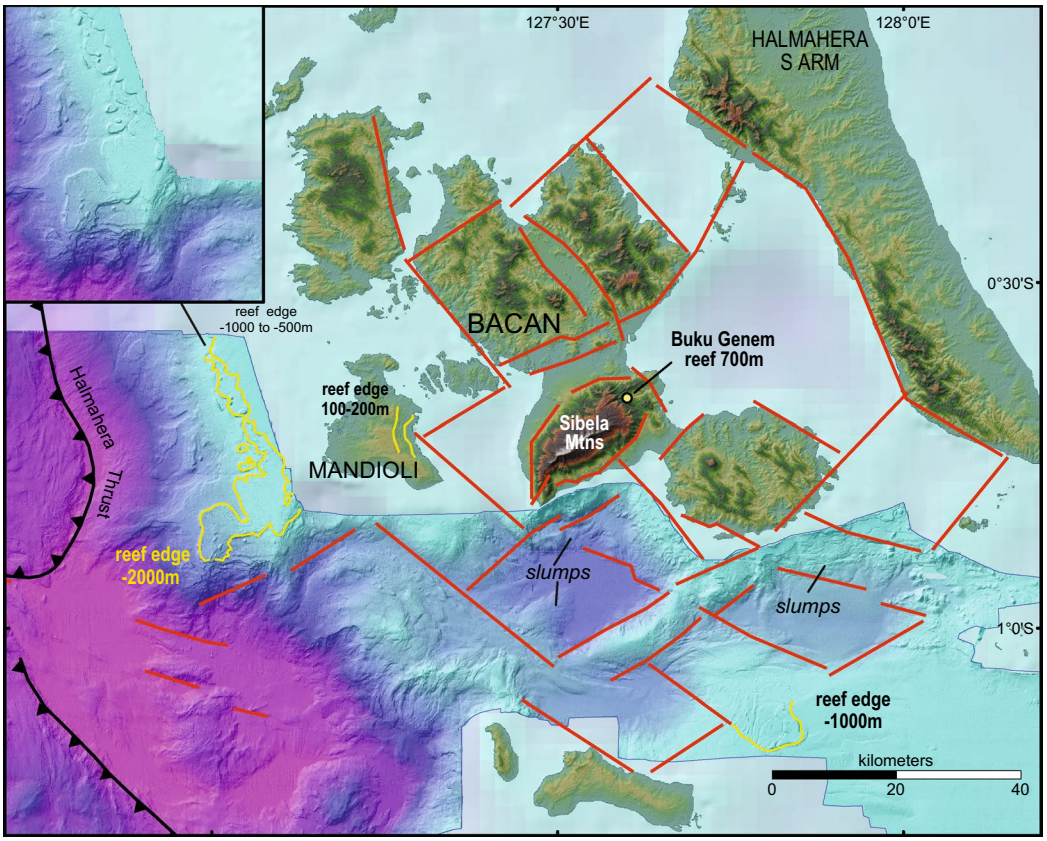

Fig. 4 The Bacan region showing major faults bounding elevated and subsided blocks and highlighting reef edges identified onshore and offshore in yellow. Inset map (top left) shows detail of offshore reefs west of Mandioli

of the adjacent offshore basin (Figs. 1b and 5a). Mapping using SRTM and multibeam imagery shows the steep sections between the foot of the southeastern Sibela Mountains and the offshore basin to the southeast where several closely spaced sub-parallel faults can be identified. The faults are associated with large vertical displacements (Fig. 5b), and the total elevation difference from the Sibela Mountains summit to the coastal alluvial fans is c. 1.7 km, and that between the summit and the adjacent offshore basin floor to the southeast is c. 4.6 km. They are interpreted as steeply-dipping normal faults (Supplements 3F, G).

The pattern of faulting and the shapes of basins contrast markedly with fault patterns and basin shapes associated with the Sorong Fault strands. The Sorong Fault basins are narrow, elongate parallel to the fault strands, and although locally up to 2 km deep are small in area (Fig. 2; Supplement 3c, d and e). In contrast, the area of the rectilinear faulting with blocks in and around Bacan is approximately 100×100 km, with basins approximately 20×20 km, compared to the approximately 25×5 km area of the largest basin in the Sorong Fault zone SE of the south arm of Halmahera (Figs. 2 and 4). Other basins associated with the Sorong Fault to the east are also narrow and elongate, approximately parallel to the E-W trend of the major fault, smaller and less deep.

Offshore there is also striking evidence of young deformation. As noted above, there are coral reefs at 700 m elevation in the NE part of the Sibela Mountains at Buku Genem and on the island of Mandioli, west of the Sibela block, former Quaternary reef edges are now at elevations of 100 to 200 m (Fig. 4). However, only 10 km west of Mandioli island, water depths increase westwards to more than 4 km, and former reefs are now drowned and distinctive reef edges are traceable at depths of 500–2000 m depth for distances of more than 30 km from north to south (Fig. 4). The reefs are not covered by significant sediment implying that the drowning is very young. Thus, from east to west, from south Halmahera crossing the Sibela Mountains to the Halmahera Thrust (Fig. 5a) is a young flexure which is deepest at the Halmahera Thrust in the west with a maximum elevation of 2 km in the central Sibela Mountains (Fig. 5b). The downfaulted basins have the form of keystone blocks within a flexural bulge. The pattern suggests the flexure and the chocolate block pattern of blocks is a consequence of loading at the Halmahera Thrust by

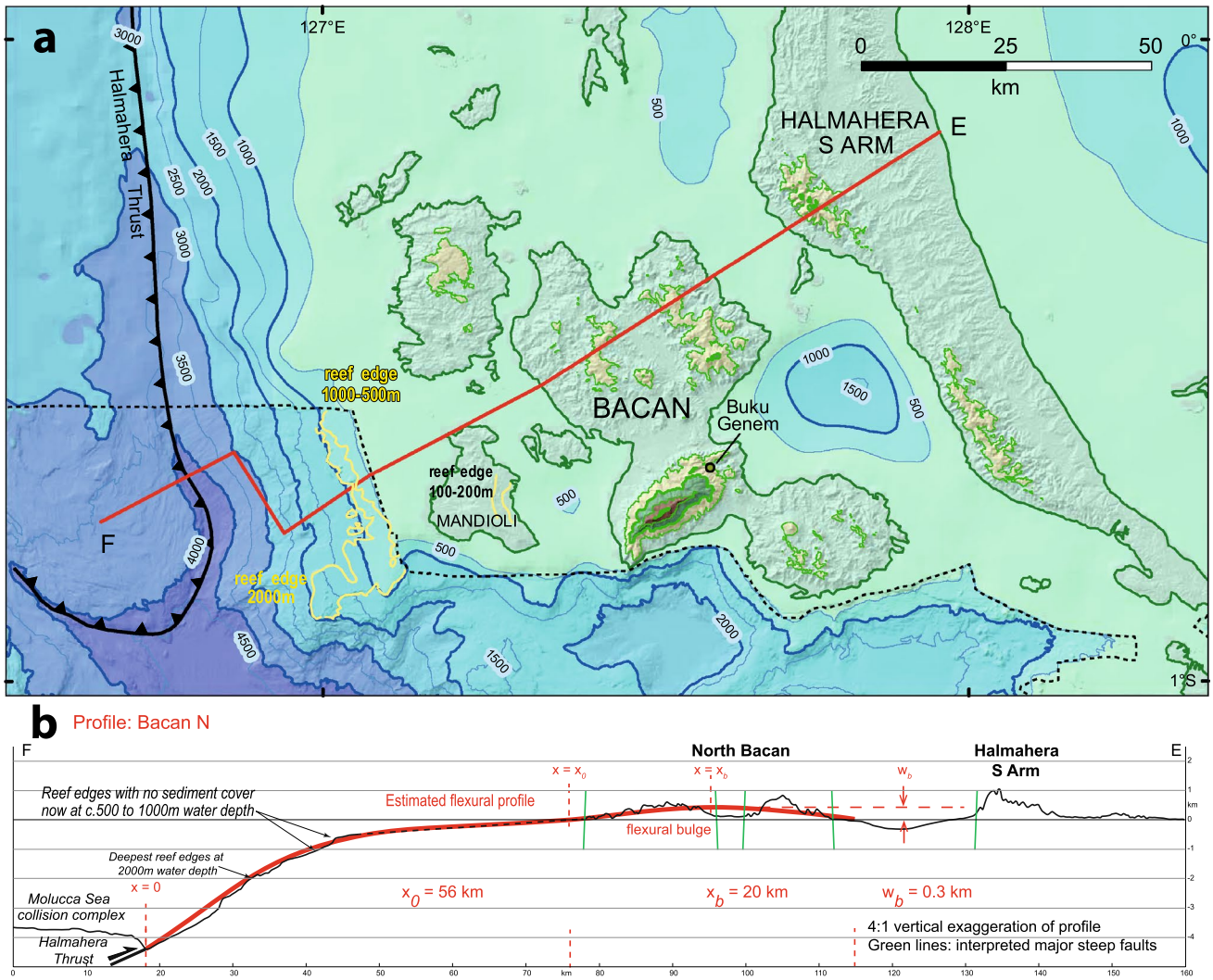

Fig. 5 **a** Simplified version of the topography and bathymetry based on the same sources as Fig. 3. The red line E–F is the elevation profile shown in **b** running from the Halmahera Thrust in the west to the Halmahera South Arm in the east. **b** Elevation profile showing the proposed flexural bulge on Bacan (red line) with parameters used for elastic thickness calculations, following the approach described by Turcotte and Schubert (2002). Elevation profile with 4 × vertical exaggeration. Green lines indicate the interpreted major steep faults that intersect the profile

the Molucca Sea collision complex (Silver and Moore 1978; Hamilton 1979; Watkinson et al. 2011).

Petrography

The staurolite-garnet schists contain quartz, feldspar, biotite, white mica, garnet, staurolite, tourmaline, an opaque phase, and rare kyanite. They have a clear foliation marked by graphite-rich white mica bands and show evidence of ductile deformation by micro-folds and shear bands. Abundant prismatic staurolite and garnet with complex internal structures grew during deformation, while relict kyanite appears to have grown during an earlier phase of metamorphism (Fig. 6a–d). White mica from the foliation bands and some white mica flakes from syn-kinematic garnet porphyroblasts and their pressure shadows have been analysed for $^{40}Ar/^{39}Ar$ from 31H and 34B to date the latest deformation event. Biotite schists are fine-grained and show biotite mica fish in an SC shear fabric (Fig. 6e). Biotite flakes from foliation, from mica fish and subordinate from SC shear fabrics have been analysed with $^{40}Ar/^{39}Ar$ from 31E for evaluation of the deformation history.

The foliated biotite-gneisses 31B and 31G-D are composed of quartz, K-feldspar, plagioclase, biotite, titanite, an opaque phase, and retrograde chlorite and epidote (Fig. 6f). The calc-silicate gneiss sample 33B contains subordinate biotite only and has abundant calcite in the foliation bands

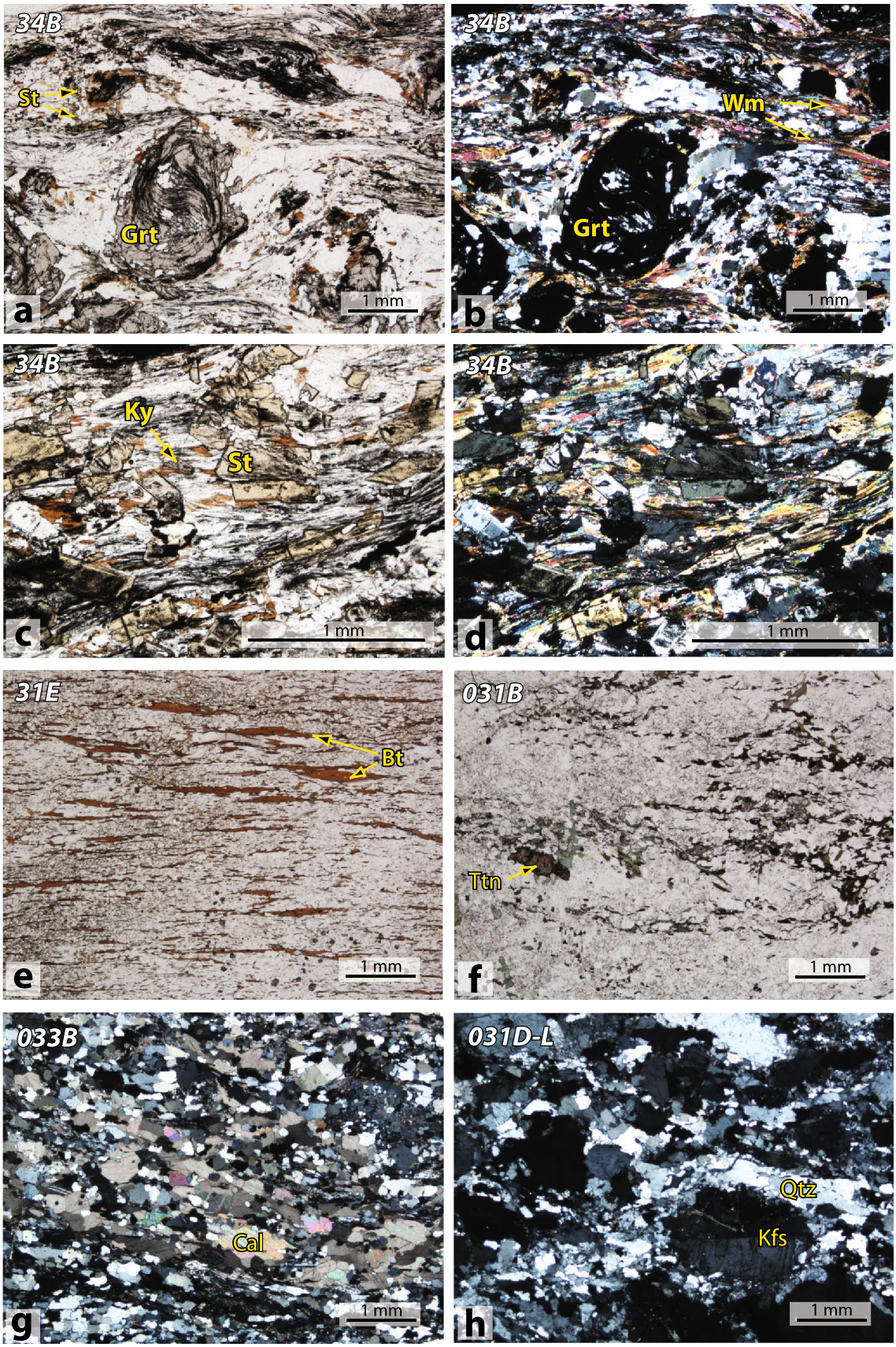
34B
St
Grt
1 mm
a
34B
Wm
Grt
1 mm
b
34B
Ky
St
1 mm
c
34B
1 mm
d
31E
Bt
1 mm
e
031B
Ttn
1 mm
f
033B
Cal
1 mm
g
031D-L
Qtz
Kfs
1 mm
h

◂**Fig. 6** Photomicrographs of metapelites, granite-gneisses and a granite dyke from the Sibela Continental Suite. **a-d** Syn-kinematic garnet porphyroblasts (**a**, **b**) and prismatic staurolite (**c**, **d**) within strongly deformed quartz and white mica bands in staurolite-garnet schist. **e** Flattened biotite flakes and biotite mica fish in SC shear fabric of biotite schist. **f** Granite-gneiss showing local retrograde alteration of biotite to chlorite. **g** Calc-silicate gneiss with recrystallized quartz and calcite bands. **h** Leucocratic granite dyke similar to 31G-L with localized quartz recrystallisation. *Bt* biotite, *Cal* calcite, *Grt* garnet, *Kfs* K-feldspar, *Ky* kyanite, *Qtz* quartz, *St* staurolite, *Ttn* titanite, *Wm* white mica

(Fig. 6g). A leucocratic granite dyke (31G-L) cross-cuts the gneiss 31G-D and contains predominantly quartz, K-feldspar and plagioclase, with local dynamic recrystallization of quartz grains (Fig. 6h).

Analytical results

Zircon U–Pb and oxygen isotopes

Zircon U–Pb and oxygen isotope analyses were undertaken on three gneisses (31B, 31G-D and 33B) and one granite dyke (31G-L). Ion microprobe analyses of zircons from gneisses 31B and 31G-D yielded Permo-Triassic ages (weighted means at 248.6 ± 2.4 Ma and 250.9 ± 3.2 Ma) from oscillatory zoned euhedral to subhedral grains (Fig. 7a, b; Supplement 2). Sample 33B also contained Permo-Triassic ages from euhedral to subrounded oscillatory zoned zircons (weighted mean at 257.2 ± 3.0 Ma), as well as Paleoproterozoic and Archean ages from subrounded to rounded zircons (Fig. 7c, d; Supplement 2). Precambrian zircons have mainly oscillatory zoned cores with dark rims or irregular overprinting structures but yielded no significant age variations between cores and rims (age differences are in the order of tens of Myrs) (Supplements 1.1 and 2).

Analysis of zircon grains from a granite dyke (31G-L) that cross-cuts 31G-D also yielded Permo-Triassic ages within oscillatory zoned zircons and grain cores (weighted mean at 251.9 ± 2.7 Ma) similar to 31G-D (Supplement 2), but in contrast Pleistocene ages (weighted mean at 1.42 ± 0.03 Ma) have been recorded within dark or oscillatory zoned grain rims (Fig. 7e, f; Supplement 2). The Th/U ratios of the Pleistocene rims are very low (0.00–0.06). Such ratios have been considered to represent metamorphic zircon growth (Ahrens et al. 1967), although this interpretation has been challenged more recently as there are also magmatic zircons with such low ratios (Yakymchuk et al. 2018).

To further characterize the different zircon ages *in-situ* oxygen isotopic analyses of the granitic dyke 31G-L were collected using SHRIMP-SI which yielded comparable $\delta^{18}O$ values from both Permo-Triassic cores (5.21–6.13 ‰) and Pleistocene rims (4.72–5.22 ‰) (Supplement 1.2). The values suggest interaction with a mantle fluid, rather than a magmatic, metamorphic or crustal source (Valley 2003; Black et al. 2004).

Mica $^{40}Ar/^{39}Ar$

$^{40}Ar/^{39}Ar$ analyses were carried out on three schistose samples (31E, 31H and 34B) from a 63–250 µm mica fraction which includes the largest mica flakes in the rocks that define the pervasive foliation (Fig. 6a-e). White mica from two staurolite-garnet schists yielded $^{40}Ar/^{39}Ar$ plateau ages of 0.79 ± 0.04 Ma (31H) and 0.69 ± 0.05 Ma (34B) (Fig. 8a, b). Biotite from biotite schist 31E yielded a plateau age of 0.64 ± 0.02 Ma (Fig. 8c). The ages indicate generally cooling through moderate (c. 300–500 °C) temperatures (Harrison et al. 1985; Reiners et al. 2018) and suggest very young exhumation in the Pleistocene.

Apatite (U–Th–Sm)/He

Multiple analyses were carried out on multi-grain aliquots from samples 31G-D (biotite-gneiss) and 31G-L (granite dyke). Five analyses of 31G-D yielded corrected ages of 0.42–1.20 Ma; three analyses of 31G-L yielded corrected ages of 0.57–0.79 Ma. Data reduction yielded weighted mean ages of 0.68 ± 0.34 Ma and 0.69 ± 0.33 Ma, respectively (95% confidence level—see Supplement 1.5). These ages are interpreted to be related to cooling through c. 70–95 °C (Wolf et al. 1996; Reiners et al. 2018), and record near-surface exhumation in the Pleistocene.

Discussion

Protoliths of the metamorphic rocks

The protoliths of gneisses in the Sibela Mountains are interpreted to be related to Permo-Triassic arc magmatism. Zircon U–Pb weighted mean ages are summarized in Table 2. Permo-Triassic ages obtained from euhedral and oscillatory zoned zircons (Supplement 2) from the biotite gneisses 31B and 31G-D (c. 249 and 251 Ma) are interpreted to reflect the crystallization ages of their granitoid protoliths. Abundant elongate to subrounded Permo-Triassic zircons and subrounded to rounded Precambrian zircons from the calc-silicate gneiss 33B (Supplement 2) are interpreted as detrital, indicating a volcaniclastic origin for the protolith. The Permo-Triassic zircons from this sample are oscillatory zoned (Supplement 2) and interpreted as ash fall deposits and/or reworked from contemporaneous Permo-Triassic magmatic rocks.

The Permo-Triassic granitoid and volcaniclastic protoliths from Bacan are interpreted to have formed during Permo-Triassic arc-related magmatism at the north Australian margin

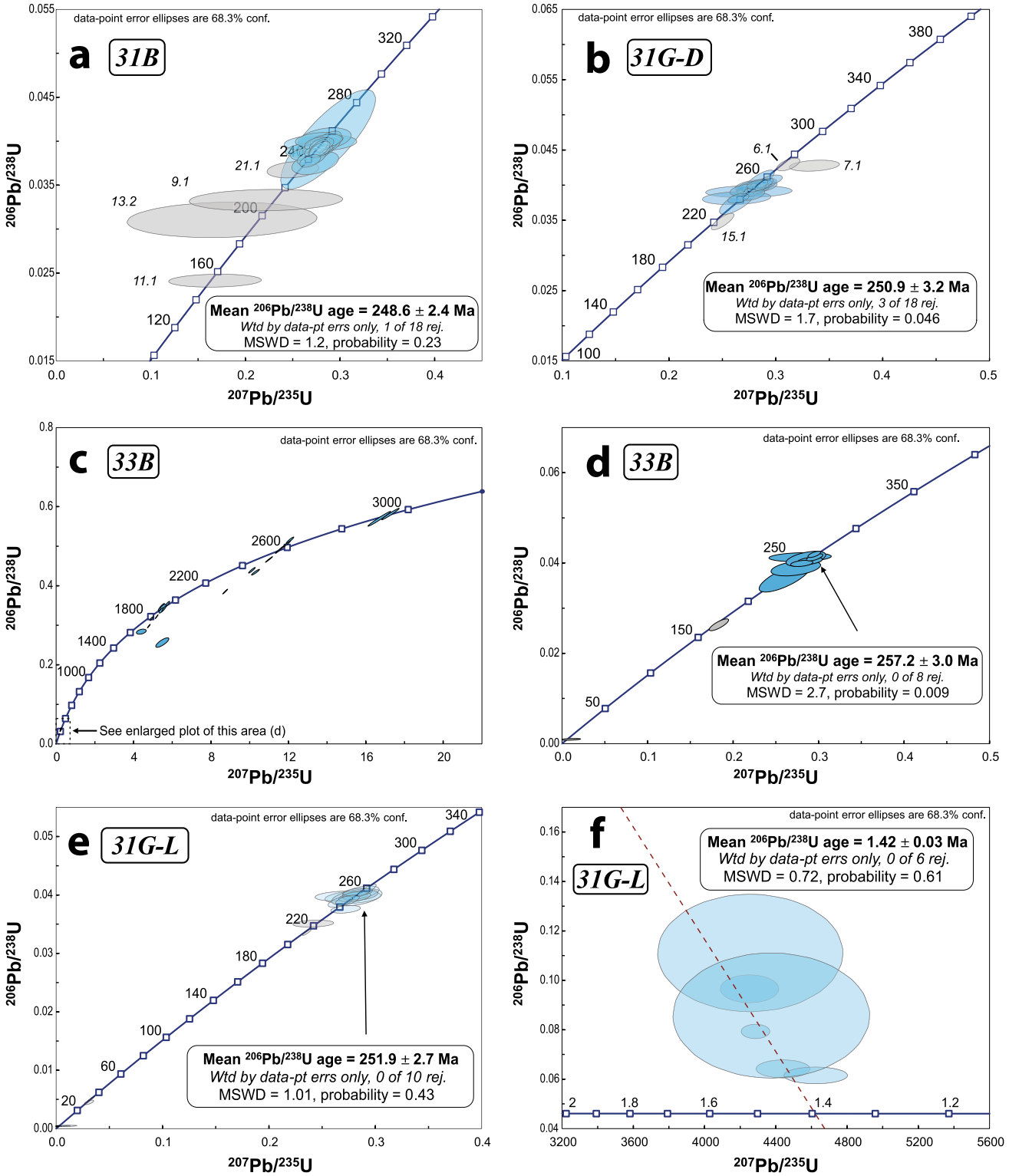

Fig. 7 Wetherill Concordia (**a**–**e**) and Tera-Wasserburg Concordia (**f**) diagrams of U–Pb zircon analyses of gneisses (**a**–**d**) and a granite dyke (**e**, **f**). All rocks analyzed contain a main Permo-Triassic zircon population. The calc-silicate gneiss yielded several zircons with Proterozoic and Archean ages (**c**), and the granite dyke recorded Pleistocene zircon rims (**f**)

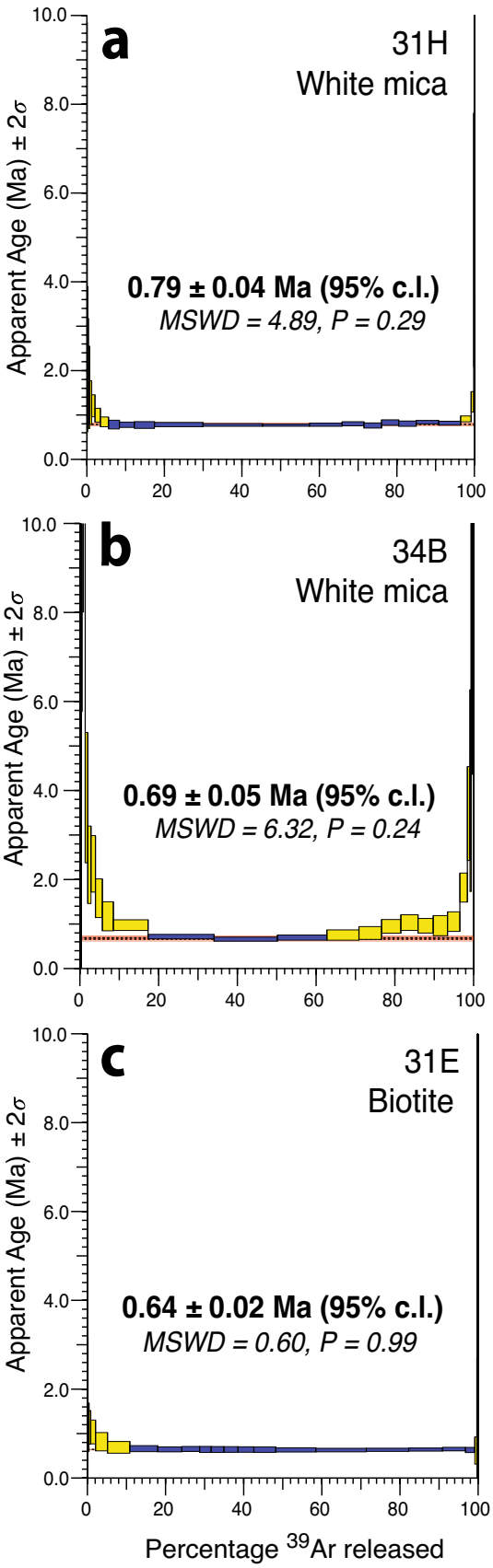

Fig. 8 $^{40}Ar/^{39}Ar$ spectra of step-heating experiments on white mica (**a, b**) and biotite (**c**) from schists showing flat plateaux, indicating very fast and very recent cooling. Blue – steps included in the age plateaux; yellow – steps not included in the age plateaux; red line – steps used for age calculation

of New Guinea (e.g. Bladon 1988; Pieters et al. 1983; Hill and Hall 2003; Gunawan et al. 2012, 2014; Zimmermann and Hall 2016). This is because similar Permo-Triassic zircons (c. 205–275 Ma) have been reported from western New Guinea from detrital zircons obtained from volcaniclastic sediments of the Tipuma Formation (Gunawan et al. 2014), and from zircon dating of Upper Permian to Upper Triassic (c. 213–257 Ma) granitoids (Webb and White 2016; Jost et al. 2018), which represent potential unmetamorphosed equivalents of the protoliths at the northern Australian margin. The age of metamorphism of this granitic basement in Bacan is not known but is possibly related to arc-continent collision in the Early Miocene.

At the time of emplacement, the Bacan Permo-Triassic granitoid melts must have intruded into a pre-Permian basement, such as the Silurian-Devonian metasediments in West Papua (Pieters et al. 1990; Jost et al. 2020) to account for the Precambrian detrital zircons found in sample 33B. The observed rounded Precambrian zircons are interpreted to be recycled from continental crust which probably forms the Precambrian basement of western New Guinea.

The granite dyke (31G-L) zircons from Bacan show the same Permo-Triassic age population as the biotite gneisses (Fig. 7e). This is interpreted as inheritance and shows that the dyke was derived from partial melting of Permo-Triassic granitoids (e.g., equivalents of its host rock 31G-D). Zircon rims from the dyke are interpreted to have crystallized at c. 1.4 Ma (Table 2) as overgrowth derived from melting. The concentric zoning (Supplement 2) and the oxygen isotope values indicate a magmatic origin despite their low Th/U ratios. The dykes show localized dynamic recrystallization as observed in the thin section (Fig. 6h) which may be related to post-crystallisation metamorphism at c. 0.7 Ma recorded in micas from schists in this study (Fig. 8) related to uplift and extension. An alternative explanation for the different metamorphic character of the dykes and the host rock gneiss is compositional differences. Deformation in both could be a result of the Pleistocene metamorphism dated in the schists, but while the gneiss with high content of mica developed a clear foliation, the leucocratic dykes only show the observed dynamic recrystallisation. This would however imply metamorphism of the granitic basement in the Pleistocene and not in the Miocene.

Table 2 Summary of radiometric ages obtained in this study

Sample	Lithology	Mineral	[a]Zircon U–Pb	[b]Mica $^{40}Ar/^{39}Ar$	[a]Apatite (U–Th–Sm)/He
31H	Staurolite-garnet schist	White mica		0.79 ± 0.04 Ma	
34B	Staurolite-garnet schist	White mica		0.69 ± 0.05 Ma	
31E	Biotite schist	Biotite		0.64 ± 0.02 Ma	
31B	Biotite-gneiss	Zircon	248.6 ± 2.4 Ma		
31G-D	Biotite-gneiss	Zircon, apatite	250.9 ± 3.2 Ma		0.68 ± 0.34 Ma
31G-L	Granite dyke	Zircon, apatite	1.42 ± 0.03 Ma		0.69 ± 0.33 Ma
33B	Calc-silicate gneiss	Zircon	257.2 ± 3.0 Ma		

1σ error for all analysis

[a]Weighted mean age

[b]Plateau age

Cooling and exhumation histories

U–Pb ages from oscillatory zoned rims on Permo-Triassic zircons in the granite dyke show they crystallized at c. 1.4 Ma (Fig. 7f) and are interpreted to represent the intrusion age of the dyke. $^{40}Ar/^{39}Ar$ dating of micas in schists record ages between c. 0.64 and 0.79 Ma (Fig. 8; Table 2) related to exhumation. Granite dykes show localized dynamic recrystallisation in thin section (Fig. 6h) which may be related to the Quaternary metamorphic ages recorded in the micas of the schists. This is interpreted to record young exhumation of the Sibela metamorphic rocks with the dyke formation related to magmatism shortly prior to exhumation.

U–Pb zircon and apatite (U–Th–Sm)/He ages from the granite dyke (31G-L), summarized in Table 2, indicate a rapid cooling history between c. 1.4 Ma and c. 0.7 Ma, recording an apparent cooling rate of 1380 °C/Ma (Fig. 9). This assumes approximate closure temperatures of 900 °C for the zircon U–Pb age and 70 °C for the apatite (U–Th–Sm)/He age (Reiners et al. 2018). Whilst the early part of this history may relate to post-emplacement cooling to ambient crustal temperatures, we interpret the rapid cooling to low temperatures to reflect exhumation of the sample in the upper crust. The lower temperature part of the cooling history can be more certainly assigned to exhumation through the upper crust. By using the apatite (U–Th–Sm)/He data (age range of c. 0.4–1.2 Ma) and assuming a present-day surface temperature of 25 °C, a minimum cooling rate between c. 38 and 113 °C/Ma can be calculated (an average of 65 °C/Ma using the average (U–Th–Sm)/He age of c. 0.69 Ma) for exhumation in the uppermost part of the continental crust (Fig. 9). An average rate of 65 °C/Ma would be high for shallow subsurface levels and exceeds rates of temperature changes during mountain uplift and exhumation achieved solely as a consequence of erosion, such as those reported, for example, from Cascadia, USA with average rates of 15 °C/Ma (Brandon et al. 1998; Reiners and Brandon 2006) or late-stage metamorphic core complex

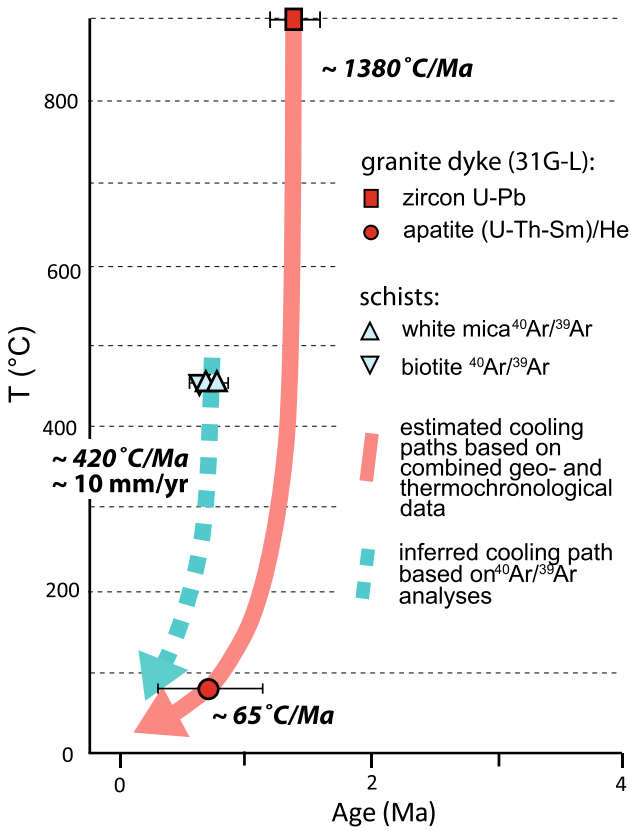

Fig. 9 Temperature versus Time plot for the granite dyke 31G-L and schists analyzed in this study. The Pleistocene geo- and thermochronological results presented in this study indicate rapid cooling and exhumation to the near-surface

exhumation, for example, of the Middle Miocene Rechnitz metamorphic core complex in the Austrian Alps at c. 11 °C/Ma (Dunkl and Denémy 1997). Thus, the cooling rate estimated for Bacan is interpreted here to indicate a different mechanism, tectonically-driven exhumation, which can facilitate such a high rate of cooling.

$^{40}Ar/^{39}Ar$ mica ages of the Sibela Mountains schists are Pleistocene (c. 0.7 Ma) (Fig. 8; Table 2) and record cooling through temperatures of c. 525 °C (phlogopite) and c. 460 °C (white mica) following Reiners et al. (2018), who calculated closure temperatures as a function of cooling rate. The apatite (U–Th–Sm)/He data of the gneiss and granite dyke indicate a geothermal gradient of c. 42 °C/km based on the software *AGE2EDOT* (Brandon et al. 1998), which suggests exhumation from an inferred maximum depth of c. 11 km. Calculation of the cooling rate using the oldest $^{40}Ar/^{39}Ar$ age of 0.83 Ma (sample 31H; plateau age plus error) and a minimum white mica closure temperature of 350 °C (Purdy and Jäger 1976; Harrison et al. 2009) with a present-day surface temperature of 25 °C, results in a cooling rate of c. 420 °C/Ma. This rate can be translated into an exhumation rate of c. 10 mm/year (Fig. 9). It should be noted that the cooling paths shown in Fig. 9 are approximations since they include uncertainties in the closure temperatures of the isotopic systems, as well as in the geothermal gradient used for calculations. However, it is clear that the very young $^{40}Ar/^{39}Ar$ ages obtained from step-heating profiles shown in Fig. 8 indicate exceptionally fast cooling and exhumation since the Pleistocene. A high heat flow due to tectonic processes and a present-day elevated geothermal gradient is supported by fault-related Quaternary volcanism in Bacan and boiling hot water springs at the eastern edge of the Sibela Mountains. Thus, cooling rates of the order of several hundred °C/Ma as calculated from the $^{40}Ar/^{39}Ar$ data are considered realistic.

The geochronological data show rapid young exhumation of continental basement in the Sibela Mountains and we suggest that the extreme differences in elevation, with rapid subsidence associated with basin formation offshore, is very young, and formed in the last 2 million years. The lack of metamorphic debris in Upper Pliocene clastic sediments, the subsidence of carbonate reefs offshore to depths up to 2 km and the uplift of reefs on land to 700 m support this interpretation. Pleistocene exhumation resulted in the erosion of metamorphic rocks and granitoids on the NW and SE side of the Sibela Mountains which formed alluvial fans at the coast, and sediments were carried offshore into the basin, manifested in places by large-scale slumps identified on the multibeam imagery (Figs. 4; Supplement 3a, b).

Uplift mechanism

The continental metamorphic rocks of the Sibela Mountains include Permo-Triassic granitoid protoliths intruded into Precambrian basement rocks or Paleozoic sedimentary cover rocks within the north Australian continental margin. These rocks were thrust beneath Philippine Sea plate arc rocks during the arc-continent collision in the Early Miocene (Fig. 10a), probably metamorphosed in that process, and formed part of the basement at the southern end of the Neogene intra-oceanic Halmahera volcanic arc (Morris et al. 1983; Forde 1997) during east-dipping subduction (Fig. 10b). The rectilinear faults were structures that predate, or were formed during the collision and later influenced location of igneous activity on Bacan, either post-collisional granite magmatism or Molucca Sea subduction-related Halmahera arc volcanism.

The east-dipping Halmahera subduction zone was initiated in the Middle Miocene forming the double subduction zone (Fig. 10b). Westward subduction rollback gradually eliminated the Molucca Sea plate since then. The Bacan region was largely submerged during the Miocene and Pliocene with Upper Miocene and Pliocene volcanism indicated by intercalated volcaniclastic material in shallow marine sediments. The Neogene and Quaternary volcanic arc was situated in east Bacan, which would have led to a high heat flow and steep geothermal gradient beneath the arc. Rollback would have led to thinning of the crust and lithosphere in the Halmahera forearc in western Bacan and further west, augmenting heat flow due to the inflow of hot mantle below the extending forearc. As the two arcs began to collide, the eastward thrusting of the Sangihe forearc over the Halmahera forearc at the Halmahera Thrust (Hall 2000; Hall and Smyth 2008) formed the Molucca Sea collision complex which loaded the Halmahera forearc in the Bacan region (Fig. 10c). There are two plausible explanations of the observed rapid and very young exhumation of the Sibela Mountains metamorphic complex, one related to vertical movement along the Sorong strike-slip system and the other to eastward thrusting of the collision complex. The loading produced a flexure with subsidence of the crust in the west, as indicated by carbonate reefs visible on the multibeam images to depths of c. 2 km (Fig. 4), and uplift further east shown by elevation of Quaternary reefs. The shape of the flexure can be assessed from bathymetric-topographic profiles across the forearc and arc and the most complete profile crosses from North Bacan to the Halmahera Thrust (Fig. 5). The elastic thickness of the plate can be estimated using the universal lithospheric deflection profile for a vertical end load (Turcotte and Schubert 2002) such as would be produced by thrusting of the collision complex onto the forearc at the Halmahera Thrust. The elastic thickness (Te) calculated from the measured height of the forebulge (w_b) and the half-width of the forebulge (x_b) is 7–10 km. Most of Indonesia has Te values less than 30 km (Tesauro et al. 2012) consistent with regionally hot and weak lithosphere (Hall and Morley 2004). The Okinawa Trough in a backarc setting has an effective elastic thickness of 9–30 km (Xu and Chen 2021). Values less than 20 km are common in the hot Cordillera backarc regions of North America (Hyndman et al. 2009) and values less than 10 km are reported for the Basin and Range area of the central U.S. Cordillera (Lowry

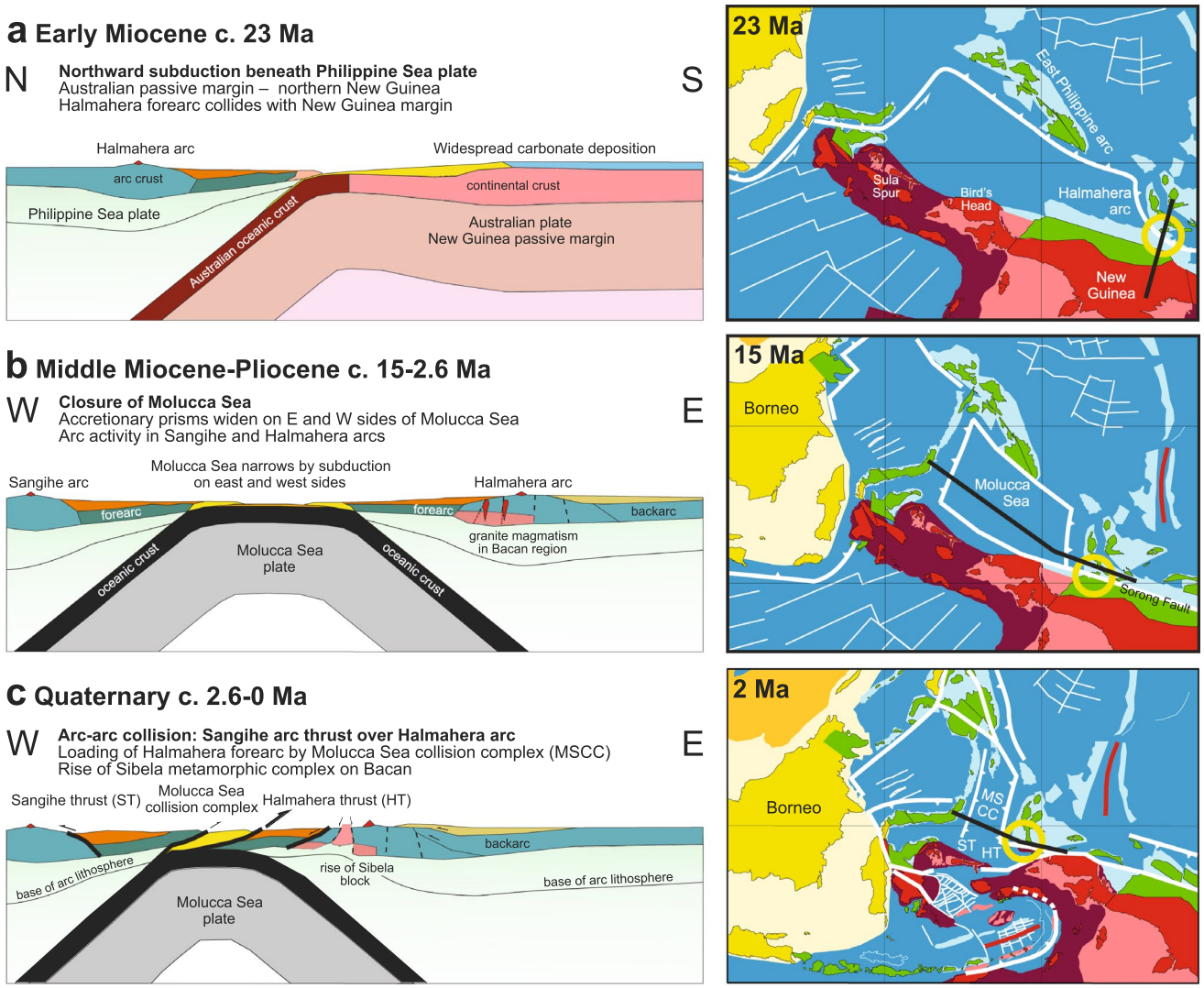

Fig. 10 Schematic cross-sections and paleogeographic maps showing the tectonic evolution of the Bacan area from the Early Miocene to Pleistocene based on Hall (2000, 2012) and Hall and Smyth (2008). Black lines on the paleogeographic maps indicate cross-section orientation; yellow circles show the location of Bacan at that time. **a** Northward subduction beneath Philippine Sea plate in the Early Miocene. **b** Closure of Molucca Sea in the Middle Miocene to Pliocene. **c** Arc-arc collision: Sangihe arc thrust over Halmahera arc in the Quaternary

and Smith 1995). The values of Te for Bacan are therefore low, but not unexpected, for an arc region in which there has been a recent extension.

This flexure of this weak lithosphere is interpreted to have reactivated the rectilinear normal faults allowing independent block movements, i.e. uplift of the Sibela Mountains and subsidence of adjacent basins. A link to the Sorong strike-slip fault system seems very unlikely. We suggest these vertical movements resulted either from the flow of the deep crust or mantle from subsided to elevated blocks (Hall 2011), or delamination of a fluid-weakened lithospheric mantle and localized upwelling of the asthenosphere (cf. Zandt et al. 2004). The former was interpreted by Morley and Westaway (2006) as a driving mechanism for subsidence in the Pattani and Malay basins. This would explain i) the heat for metamorphism recorded by the $^{40}Ar/^{39}Ar$ cooling ages, ii) growth of high-temperature Buchan-type metamorphic minerals (staurolite, garnet), iii) granite dyke magmatism from re-melting of the basement, including $\delta^{18}O$ mantle signatures, and iv) Quaternary andesitic volcanoes and volcanic rocks along the rectilinear faults around the Sibela Mountains. All of these features have similarities to metamorphic core complexes (MCC); however, the interpreted high-angle nature of the faults is different from the classic MCC model which is characterized by low-angle detachment faults. Furthermore, there is no indication of a major mylonitic shear zone although this could be obscured by rainforest.

We suggest that vertical movements along block-bounding normal faults facilitated rapid exhumation coupled with rapid subsidence of adjacent basins. We propose that this type of steep fault-controlled complex be termed a metamorphic block complex (MBC). This study invites the search for similar complexes in rapidly exhumed regions elsewhere.

Analogous metamorphic complexes

The extreme exhumation of Plio-Pleistocene metamorphic blocks is relatively poorly documented around the world. There are other metamorphic complexes in east Indonesia, in NW Sulawesi and Seram, some interpreted as classic metamorphic core complexes (e.g., Baldwin et al. 1993; Little et al. 2007; Spencer 2011; van Leeuwen et al. 2016; Advokaat et al. 2017), whereas others have similarities to the Bacan metamorphic rocks having been rapidly exhumed with young high-grade metamorphic rocks and granites within steep fault zones. We look at two examples in SE Asia and discuss the similarities.

In NW Sulawesi the Palu Metamorphic Complex (PMC) was exhumed in the Pliocene (van Leeuwen and Muhardjo 2005; van Leeuwen et al. 2016; Hennig et al. 2017). Schists containing andalusite, cordierite, staurolite and Mn-rich garnet are associated with granite gneisses. $^{40}Ar/^{39}Ar$ dating of biotite, white mica and amphibole from strongly deformed mylonitic schists and recrystallized amphibolites reveals Early Pliocene (c. 5.3–4.8 Ma) cooling in the northern part and Late Pliocene (c. 3.1–2.7 Ma) cooling in the southern part of the PMC (Hennig et al. 2017). U–Pb, $^{40}Ar/^{39}Ar$ and (U–Th–Sm)/He analyses of various minerals from PMC metamorphic and S-type magmatic rocks give very similar mid to Late Pliocene ages. A minimum cooling rate of c. 17–21 °C/Ma is estimated for near-surface exhumation based on an apatite (U–Th–Sm)/He age of 2.4 ± 0.2 Ma from a granite dyke (Hennig et al. 2017). Alluvial and fluvial sediments of the Palu Formation unconformably overlie the PMC and contain Pleistocene nannofossils and alunite clasts that yielded a K–Ar age of 1.7 Ma (van Leeuwen and Muhardjo 2005; van Leeuwen et al. 2016) which indicate the PMC had reached the surface by then. A depositional age of 1.7 Ma results in a cooling rate of around 64 °C/Ma, similar to the average cooling rate proposed here for the Sibela Mountains. Exhumation of the PMC was interpreted by Hennig et al. (2017) to have been facilitated by steep faults in a major strike-slip system linked to subduction rollback at the North Sulawesi trench (Hall 2018).

Seram has a longer complex Neogene history of metamorphism and granite melting. $^{40}Ar/^{39}Ar$ and U–Pb ages from different rock types record thermal events at 25–20 Ma, 16 Ma, 5.7 Ma, 4.5 Ma, and 3.4 Ma (Pownall et al. 2017a, b). Late Oligocene–Early Miocene collision between the Australian continental crust and the north Sulawesi volcanic arc is recorded by zircon U–Pb ages. At 16 Ma, a major kyanite-grade metamorphic event in western and central Seram occurred at the same time as ultrahigh-temperature metamorphism and melting of granulite-facies rocks (Pownall et al. 2017a). These are interpreted to mark extension during slab rollback which exhumed lherzolites and adjacent granulite-facies migmatites beneath extensional detachment faults in western Seram at 6.0–5.5 Ma, heating and shearing adjacent schists to form gneisses (Pownall et al. 2017b), followed by widespread deformation and exhumation of migmatites on Ambon at c. 3.5 Ma (Pownall et al. 2017a). Ambonites, cordierite- and garnet-bearing dacites sourced predominantly from melts generated in the migmatites, were later erupted on Ambon from 3.0 to 1.9 Ma. These ages support multiple episodes of high-temperature extension and strike-slip faulting, interpreted to be the result of Seram being detached from SE Sulawesi, extended, and dragged east by the rollback of the Banda subduction hinge.

The metamorphic complexes in NW Sulawesi and Seram are largely narrow elevated zones bounded by or within strike-slip faults. The PMC on Sulawesi was rapidly exhumed along steep faults in a strike-slip setting, while the metamorphic rocks on Seram were exhumed along strands of a larger detachment fault in a strike-slip setting. Some prominent strike-slip faults reported around the world do have branch fractures combined with antithetic faults at their tips or where multiple stepping strike-slip features interact (e.g. Kim et al. 2003), but these are small and result in a series of parallel rotated blocks. Large-scale strike-slip faults can have normal faults at their tips, for example, the La Tet Fault, eastern Pyrenees (Cabrera et al. 1988), which are commonly straight and have an angle of c. 40–50° to the master fault (Kim and Sanderson 2006). Major strike-slip faults such as the Tan-Lu fault zone in eastern China (Lu et al. 2023) terminate in thrusting, fault-related folding and uplift, as well as basins, but these are quite unlike the pattern of rectilinear faults and blocks close to Bacan. Although the major Sorong strike-slip fault zone passes close to Bacan (Fig. 3), there are no major elevated fault blocks within the several narrow horsetails splays near the western end of the fault zone. Within these strands are basins which are narrow, elongate parallel to the faults, c. 10–30 km long and up to c. 5–10 km wide, and locally up to 2 km deep in which 2D seismic lines show up to 1 s TWT (two-way travel time) of sediment. The largest basin in a Sorong Fault strand SE of the south arm of Halmahera is approximately 25×5 km in area (Fig. 3). There are few important faults not parallel to the main, broadly E-W, trend of the Sorong Fault strands. The rectilinear pattern of faulting within the area in and around Bacan is very different, to both the Sorong Fault strands, as well as the PMC and Seram complexes.

Elsewhere in the world, the Rwenzori Mountains of East Africa have some similarities to the Sibela Mountains. They consist of a Precambrian metamorphic basement, now elevated

to more than 5 km, forming a horst block at the edge of the western branch of the East African Rift system (Kaufmann et al. 2016). Uplift mechanisms are still debated. Wallner and Schmeling (2011) interpreted the delamination of part of the mantle lithosphere resulting in the rebound of the crust. Sachau and Koehn (2010) and Sachau et al. (2013) interpreted fault-related uplift in a rift-related extensional setting. Bauer et al. (2013) interpreted a long exhumation history, with rock uplift since the Miocene which outpaced erosion resulting in recent high and asymmetric topography, and fast final surface uplift associated with glacial erosion along predefined fault zones. Kaufmann et al. (2016) modelled an uplift rate of 1–2 mm/year in the last 2 Ma and Bauer et al. (2013) interpreted Plio-Pleistocene surface uplift/erosion in the Rwenzori Mountains to be around < 2–3 km, which would translate into roughly 1 mm/year uplift rate, both much lower than the rates we interpret for the Sibela Mountains. During the uplift of the Rwenzori Mountains since 300 ka, Ring (2008) suggested glacial erosion removed c. 1–2 km material at rates of 1.5–4 mm/year, which are similar to those of the Sibela Mountains, leading to isostatic rebound promoting normal faulting. All studies recognize that the exhumation of the Rwenzori Mountains occurred in a continental rift setting, very different from the Sibela Mountains, although high uplift rates and steeply dipping faults have contributed to the rapid exhumation of deep crustal metamorphic rocks.

Conclusions

Eastern Indonesia is a tectonically active region in which there are many examples of rapidly exhumed metamorphic complexes. Some conventional metamorphic core complexes characterized by low-angle detachments (van Leeuwen and Muhardjo 2005; van Leeuwen et al. 2007, 2016; Spencer 2011; Advokaat et al. 2017) are potentially active today (Hall 2018). Others are bounded by steep strike-slip faults, such as the PMC in NW Sulawesi (van Leeuwen and Muhardjo 2005; van Leeuwen et al. 2016; Hennig et al. 2017), or are within strike-slip fault zones such as those of Seram (Pownall et al. 2017a, b). The Bacan MBC is a different type of steep fault-controlled metamorphic complex. It is exceptionally young and like the other east Indonesian complexes was rapidly exhumed. We propose that this type of steep fault-controlled complex be termed a metamorphic block complex (MBC). Although each listed metamorphic complex is different they have important common features: all are young, were rapidly exhumed, and were associated in different ways with subduction rollback. Exhumation rates for all the east Indonesian examples are much higher than those estimated for older core complexes (e.g., Whitney et al. 2013; Baran et al. 2017) and we consider the rates determined for these young complexes are probably closer to the actual speeds of metamorphic complex exhumation since rates estimated from older complexes are averages measured over longer periods of time (Hennig et al. 2017).

Supplementary Information The online version contains supplementary material available at https://doi.org/10.1007/s00531-024-02390-1.

Acknowledgements This study was funded by the SE Asia Research Group at Royal Holloway, University of London. We thank TGS and GeoData Ventures Pte Ltd for the use of their multibeam bathymetry data; Sam Melia assisted with the preparation of maps. $^{40}Ar/^{39}Ar$ dating was supported by ANU Argon facility ARC grant number (DP120103554). The apatite-He thermochronology analyses were funded by an internal grant awarded to LTW from the Faculty of Science, Medicine and Health at the University of Wollongong. The University of Melbourne Thermochronology Laboratory receives infrastructure support under the AuScope program of the Australian National Collaborative Research Infrastructure Strategy (NCRIS). Mike Cottam and Olivier Vanderhaeghe provided useful comments on earlier versions of the manuscript. We thank Chris Morley and an anonymous reviewer for their helpful comments.

Author contributions Conceptualization: Juliane Hennig-Breitfeld, Robert Hall, Lloyd White. Data acquisition and data analysis: Marnie Forster, Richard Armstrong, Barry Kohn, Lloyd White, Tim Breitfeld. Interpretation of data: Juliane Hennig-Breitfeld, Robert Hall. Writing—original draft: Juliane Hennig-Breitfeld, Robert Hall. Writing—review and editing: Robert Hall, Juliane Hennig-Breitfeld, Tim Breitfeld, Lloyd White, Marnie Forster, Barry Kohn.

Funding Open Access funding enabled and organized by Projekt DEAL.

Data availability All data used in the manuscript are available in Supplementary Table 1.1–1.5.

Declarations

Conflict of interest The authors declare that they have no competing financial interests or personal relationships that could have appeared to influence the work reported in this paper.

References

Advokaat EL, Hall R, White LT, Watkinson IM, Rudyawan A, BouDagher-Fadel MK (2017) Miocene to recent extension in NW Sulawesi, Indonesia. J Asian Earth Sci 147:378–401. https://doi.org/10.1016/j.jseaes.2017.07.023

Ahrens LH, Cherry RD, Erlank AJ (1967) Observations on the Th-U relationship in zircons from granite rocks and from kimberlites. Geochim Cosmochim Acta 31:2379–2387. https://doi.org/10.1016/0016-7037(67)90009-9

Baker SJ, Malaihollo JFA (1996) Dating of Neogene igneous rocks in the Halmahera region: arc initiation and development. In: Hall R, Blundell DJ (eds) Tectonic Evolution of Southeast Asia, vol 106. Geological Society of London Special Publication, pp 483–497. https://doi.org/10.1144/GSL.SP.1996.106.01.31

Baldwin SL, Lister GS, Hill EJ, Foster DA, McDougall I (1993) Thermochronologic constraints on the tectonic evolution of active metamorphic core complexes, D'Entrecasteaux Islands. Papua New Guinea. Tectonics 12(3):611–628. https://doi.org/10.1029/93TC00235

Baran ZO, Dilek Y, Stockli D (2017) Diachronous uplift and cooling history of the Menderes core complex, western Anatolia (Turkey), based on new Zircon (U-Th)/He ages. Tectonophysics 694:181–196. https://doi.org/10.1016/j.tecto.2016.12.005

Bauer FU, Glasmacher UA, Ring U, Karl M, Schumann A, Nagudi B (2013) Tracing the exhumation history of the Rwenzori Mountains, Albertine Rift, Uganda, using low-temperature thermochronology. Tectonophysics 599:8–28. https://doi.org/10.1016/j.tecto.2013.03.032

Bladon GM (1988) Preliminary geological report. Catalogue, appraisal and significance of K-Ar isotopic ages determined for igneous and metamorphic rocks in Irian Jaya. Indonesia-Australia Geological Mapping Project, pp 79

Becker JJ, Sandwell DT, Smith WHF, Braud J, Binder B, Depner J, Fabre D, Factor J, Ingalls S, Kim S-H, Ladner R, Marks K, Nelson S, Pharaoh A, Trimmer R, Von Rosenberg J, Wallace G, Weatherall P (2009) Global bathymetry and elevation data at 30 arc seconds resolution: SRTM30_PLUS. Mar Geodesy 32(4):355–371. https://doi.org/10.1080/01490410903297766

Beltrando M, Lister GS, Forster MA, Dunlap WJ, Fraser G, Hermann J (2009) Dating microstructures by the $^{40}Ar/^{39}Ar$ step-heating technique: deformation-pressure-temperature-time history of the Penninic units of the Western Alps. Lithos 113:801–819. https://doi.org/10.1016/j.lithos.2009.07.006

Black LP, Kamo SL, Allen CM, Davis DW, Aleinikoff JN, Valley JW, Mundil R, Campbell IH, Korsch RJ, Williams IS, Foudoulis C (2004) Improved $^{206}Pb/^{238}U$ microprobe geochronology by the monitoring of a trace-element-related matrix effect; SHRIMP, ID-TIMS, ELA-ICP-MS and oxygen isotope documentation for a series of zircon standards. Chem Geol 205:115–140. https://doi.org/10.1016/j.chemgeo.2004.01.003

Brandon MT, Roden-Tice MK, Garver JI (1998) Late Cenozoic exhumation of the Cascadia accretionary wedge in the Olympic Mountains, Northwest Washington State. Geol Soc Am Bull 110:985–1009. https://doi.org/10.1130/0016-7606(1998)110%3c0985:LCEOTC%3e2.3.CO;2

Brouwer HA (1921) (1923) Bijdrage tot de geologie van het eiland Batjan. Jaarboek Mijnwezen Nederlandsch Oost Indie Verhandelingen 50(2):76–105

Cabrera L, Roca E, Santanach P (1988) Basin formation at the end of a strike–slip fault: the Cerdanya Basin (eastern Pyrenees). J Geol Soc Lond 145:261–268. https://doi.org/10.1144/gsjgs.145.2.0261

Claoué-Long JC, Compston W, Roberts J, Fanning CM (1995) Two carboniferous ages: a comparison of SHRIMP zircon dating with conventional zircon ages and 40Ar/39Ar analysis. In: Berggren WA, Kent DV, Aubry M-P, Hardenbol J (eds) Geochronology, time scales and global stratigraphic correlation. SEPM (Society for Sedimentary Geology) Special Publication 4, pp 3–21

Dunkl I, Demény A (1997) Exhumation of the Rechnitz Window at the border of the Eastern Alps and Pannonian Basin during Neogene extension. Tectonophysics 272:197–211. https://doi.org/10.1016/S0040-1951(96)00258-2

Farr TG, Kobrick M (2000) Shuttle radar topography mission produces a wealth of data. Eos Trans AGU 81(48):583–585. https://doi.org/10.1029/EO081i048p00583

Forde EJ (1997) The geochemistry of the Neogene Halmahera Arc, eastern Indonesia. PhD thesis, University of London, pp 268

Forster MA, Lister GS (2004) The interpretation of $^{40}Ar/^{39}Ar$ apparent age spectra produced by mixing: application of the method of asymptotes and limits. J Struct Geol 26:287–305. https://doi.org/10.1016/j.jsg.2003.10.004

Forster M, Lister G (2009) Core-complex-related extension of the Aegean lithosphere initiated at the Eocene-Oligocene transition. J Geophys Res 114(B2). https://doi.org/10.1029/2007JB005382

Forster MA, Lister GS (2014) $^{40}Ar/^{39}Ar$ Geochronology and the Diffusion of ^{39}Ar in phengite-muscovite intergrowths during step-heating experiments *in vacuo*. Geol Soc Lond, Spec Publ 378:117–135. https://doi.org/10.1144/SP378.16

Gleadow A, Harrison M, Kohn B, Lugo-Zazueta R, Phillips D (2015) The Fish Canyon Tuff: a new look at an old low-temperature thermochronology standard. Earth Planet Sci Lett 424:95–108. https://doi.org/10.1016/j.epsl.2015.05.003

Gunawan I, Hall R, Sevastjanova I (2012) Age, character and provenance of the Tipuma Formation, West Papua: new insights from detrital zircon dating. In: Proceedings of the Indonesian Petroleum Association 36th Annual Convention, IPA12-G-027

Gunawan I, Hall R, Augustsson C, Armstrong R (2014) Quartz from the Tipuma Formation, West Papua: New insights from geochronology and cathodoluminescence studies. In: Proceedings of the Indonesian Petroleum Association 38th Annual Convention, IPA14-G-303

Hall R (1987) Plate boundary evolution in the Halmahera region, Indonesia. Tectonophysics 144:337–352. https://doi.org/10.1016/0040-1951(87)90301-5

Hall R (2000) Neogene history of collision in the Halmahera region, Indonesia. Proceedings of the Indonesian Petroleum Association 27th Annual Convention, pp 487–493

Hall R (2011) Australia-SE Asia collision: plate tectonics and crustal flow. In: Hall R, Cottam MA and Wilson MEJ (eds) The SE Asian Gateway: History and Tectonics of the Australia-Asia collision. Geological Society of London Special Publication 355:75–109. https://doi.org/10.1144/SP355.5.

Hall R (2012) Late Jurassic-Cenozoic reconstructions of the Indonesian region and the Indian Ocean. Tectonophysics 570–571:1–41. https://doi.org/10.1016/j.tecto.2012.04.021

Hall R (2018) The subduction initiation stage of the Wilson cycle. In: Wilson RW, Houseman GA, McCaffrey KJW, Doré AG and Buiter SJH (eds) Fifty Years of the Wilson Cycle Concept in Plate Tectonics. Geological Society of London Special Publication 470:415–437. https://doi.org/10.1144/SP470.3.

Hall R, Morley CK (2004) Sundaland Basins. In: Clift P, Wang P, Kuhnt W, and Hayes DE (eds) Continent-Ocean Interactions within the East Asian Marginal Seas. American Geophysical Union, Geophysical Monograph 149:55–85. https://doi.org/10.1029/149GM04.

Hall R, Smyth HR (2008) Cenozoic arc processes in Indonesia: Identification of the key influences on the stratigraphic record in active volcanic arcs. In: Draut AE, Clift PD and Scholl DW (eds) Formation and Applications of the Sedimentary Record in Arc Collision Zones. Geological Society of America Special Paper 436:27–54. https://doi.org/10.1130/2008.2436(03).

Hall R, Spakman W (2015) Mantle structure and tectonic history of SE Asia. Tectonophysics 658:14–45. https://doi.org/10.1016/j.tecto.2015.07.003

Hall R, Audley-Charles MG, Banner FT, Hidayat S, Tobing SL (1988) Basement rocks of the Halmahera region, Eastern Indonesia: a

Late Cretaceous-Early Tertiary arc and fore-arc. J Geol Soc Lond 145:65–84. https://doi.org/10.1144/gsjgs.145.1.0065
Hall R, Ali J, Anderson C, Baker S, Malaihollo J, Roberts S, Finch E, Agustiyanto DA, Milsom J, Nichols G (1992) The Sorong Fault Zone Project: Processes and rates of terrane amalgamation. The Sorong Fault Zone, Eastern Indonesia. SE Asia Research Group Report 111, pp 210.
Hamilton W (1979) Tectonics of the Indonesian region. U. S. Geological Survey Professional Paper 1078, pp 345. https://doi.org/10.3133/pp1078
Harrison TM, Duncan I, McDougall I (1985) Diffusion of ^{40}Ar in biotite: temperature, pressure and compositional effects. Geochim Cosmochim Acta 49:2461–2468. https://doi.org/10.1016/0016-7037(85)90246-7
Harrison TM, Célérier J, Aikman AB, Hermann J, Heizler MT (2009) Diffusion of ^{40}Ar in muscovite. Geochim Cosmochim Acta 73:1039–1051. https://doi.org/10.1016/j.gca.2008.09.038
Hennig J, Hall R, Armstrong RA (2016) U-Pb zircon geochronology of rocks from west Central Sulawesi, Indonesia: Extension-related metamorphism and magmatism during the early stages of mountain building. Gondwana Res 32:41–63. https://doi.org/10.1016/j.gr.2014.12.012
Hennig J, Hall R, Forster MA, Kohn BP, Lister GS (2017) Rapid cooling and exhumation as a consequence of extension and crustal thinning: Inferences from the Late Miocene to Pliocene Palu Metamorphic Complex, Sulawesi, Indonesia. Tectonophysics 712:600–622. https://doi.org/10.1016/j.tecto.2017.06.025
Hill KC, Hall R (2003) Mesozoic-Cenozoic evolution of Australia's New Guinea margin in a west Pacific context. Geological Soc Australia Spec Publ 22:259–283
Hyndman RD, Currie CA, Mazzotti S, Frederiksen A (2009) Temperature control of continental lithosphere elastic thickness, Te vs Vs. Earth Planet Sci Lett 277:539–548. https://doi.org/10.1016/j.epsl.2008.11.023
Jost BM, Webb M, White LT (2018) The Mesozoic and Palaeozoic granitoids of north-western New Guinea. Lithos 312:223–243. https://doi.org/10.1016/j.lithos.2018.04.027
Jost BM, Webb M, White LT, Tiranda H (2020) Regional high-T/low-P metamorphism of the Kemum Basement High, Bird's Head, West Papua, Indonesia. J Metamorph Geol 39:781–817. https://doi.org/10.1111/jmg.12586
Kaufmann G, Hinderer M, Romanov D (2016) Shaping the Rwenzoris: balancing uplift, erosion, and glaciation. Int J Earth Sci 105:1761–1778. https://doi.org/10.1007/s00531-015-1174-2
Kim YS, Peacock DCP, Sanderson DJ (2003) Mesoscale strike-slip faults and damage zones at Marsalforn, Gozo Island, Malta. J Struct Geol 25:793–812. https://doi.org/10.1016/S0191-8141(02)00200-6
Kim YS, Sanderson DJ (2006) Structural similarity and variety at the tips in a wide range of strike–slip faults: a review. Terra Nova 18:330–344. https://doi.org/10.1111/j.1365-3121.2006.00697.x
Little TA, Baldwin SL, Fitzgerald PG, Monteleone B (2007) Continental rifting and metamorphic core complex formation ahead of the Woodlark spreading ridge, D'Entrecasteaux Islands, Papua New Guinea. Tectonics 26:TC1002. https://doi.org/10.1029/2005TC001911
Lovera OM, Richter FM, Harrison TM (1989) The ^{40}Ar/^{39}Ar thermochronometry for slowly cooled samples having a distribution of diffusion domain sizes. J Geophys Res 94:17917–17935. https://doi.org/10.1029/JB094iB12p17917
Lowry AR, Smith RB (1995) Strength and rheology of the western U.S. Cordillera. J Geophys Res 100:17947–17963. https://doi.org/10.1029/95JB00747
Lu Y, Zhu G, Yin H, Wu X, Zhang S, Xie C (2023) Intracontinental deformation around the fixed tip of the continental-scale, strike-slip Tan–Lu fault zone in eastern China. J Geol Soc Lond 180:jgs2022-118. https://doi.org/10.1144/jgs2022-118
Ludwig KR (2012) User's manual for Isoplot 3.75. Berkeley Geochronology Center, Spec Publ 5, Berkeley, CA, pp. 75
Malaihollo JFA, Hall R (1996) The geology and tectonic evolution of the Bacan region, east Indonesia, In: Hall R and Blundell DJ (eds) Tectonic Evolution of Southeast Asia. Geological Society of London Special Publications 106:483–497. https://doi.org/10.1144/GSL.SP.1996.106.01.30.
Mange MA, Maurer HFW (1992) Heavy minerals in colour. Chapman and Hall, London, p 147. https://doi.org/10.1007/978-94-011-2308-2
McDowell FW, McIntosh WC, Farley KA (2005) A precise ^{40}Ar–^{39}Ar reference age for the Durango apatite (U–Th)/He and fission-track dating standard. Chem Geol 214:249–263. https://doi.org/10.1016/j.chemgeo.2004.10.002
McDougall I, Harrison TM (1999) Geochronology and thermochronology by the ^{40}Ar/^{39}Ar method. Oxford University Press, Oxford, pp. 269
Mollat H (1979) Photogeological investigations on Bacan Island (Moluccas, Indonesia), Sept. 23–Dec. 14, 1978. In: Federal Institute for Geoscience and Natural Resources, pp. 10
Moore GF, Silver EA (1983) Collision processes in the northern Molucca Sea. In: Hayes DE (ed) The tectonic and geologic evolution of southeast asian seas and islands, Part 2. Geophysical Monograph 27, American Geophysical Union, Washington, DC, pp 360–372. https://doi.org/10.1029/GM027p0360
Morley CK, Westaway R (2006) Subsidence in the super-deep Pattani and Malay basins of Southeast Asia: a coupled model incorporating lower-crustal flow in response to post-rift sediment loading. Basin Res 18:51–84. https://doi.org/10.1111/j.1365-2117.2006.00285.x
Morris JD, Jezek PA, Hart SR, Gill JB (1983) The Halmahera island arc, Molucca Sea collision zone, Indonesia: a geochemical survey. In: Hayes DE (ed) The Tectonic and Geologic Evolution of Southeast Asian Seas and Islands, Part 2, Geophysical Monograph 27, American Geophysical Union, p 373–387. https://doi.org/10.1029/GM027p0373
Orange DL, Teas PA, Decker J (2010) Multibeam backscatter—insights into marine geological processes and hydrocarbon seepage. In: OTC 20860, p. 1–22, May 2010 Offshore Technol. Conf., Houston, TX.
Pieters PE, Pigram CJ, Trail DS, Dow DB, Ratman N, Sukamto R (1983) The stratigraphy of western Irian Jaya, vol 8. Bulletin Geological Research and Development Centre, Bandung, pp. 14–48
Pieters PE, Hakim AS, Atmawinata S (1990) Geologi lembar Ransiki, Irian Jaya. Directorate of Mineral Resources, Geological Research and Development Centre, Bandung, pp. 81
Pownall JM, Hall R, Armstrong RA, Forster MA (2014) Earth's youngest known ultrahigh-temperature granulites discovered on Seram, eastern Indonesia. Geology 42:279–282. https://doi.org/10.1130/G35230.1
Pownall JM, Forster MA, Hall R, Watkinson IM (2017a) Tectonometamorphic evolution of Seram and Ambon, eastern Indonesia: Insights from ^{40}Ar/^{39}Ar geochronology. Gondwana Res 44:35–53. https://doi.org/10.1016/j.gr.2016.10.018
Pownall JM, Hall R, Armstrong RA (2017b) Hot lherzolite exhumation, UHT migmatite formation, and acid volcanism driven by Miocene rollback of the Banda Arc, eastern Indonesia. Gondwana Res 51:92–117. https://doi.org/10.1016/j.gr.2017.07.003
Purdy J, Jäger E (1976) K-Ar ages on rock-forming minerals from the central Alps: Padova, Italy. Società Cooperative Tipografica
Reiners PW, Carlson RW, Renne P, Cooper KM, Granger DE, McLean NM, Schoene B (2018) Geochronology and thermochronology. Wiley and Sons Ltd, pp. 461. https://doi.org/10.1002/9781118455876

Ring U (2008) Extreme uplift of the Rwenzori Mountains in the East African Rift, Uganda: Structural framework and possible role of glaciations. Tectonics. https://doi.org/10.1029/2007TC002176

Sachau T, Koehn D (2010) Faulting of the lithosphere during extension and related rift-flank uplift: a numerical study. Int J Earth Sci 99:1619–1632. https://doi.org/10.1007/s00531-010-0513-6

Sachau T, Koehn D, Passchier C (2013) Mountain-building under extension. Am J Sci 313(4):326–344. https://doi.org/10.2475/04.2013.03

Scott RJ, Foster DA, Lister GS (1998) Tectonic implications of rapid cooling of lower plate rocks from the Buckskin-Rawhide metamorphic core complex, west-central Arizona. Geol Soc Am Bull 110:588–614. https://doi.org/10.1130/0016-7606(1998)110%3c0588:TIORCO%3e2.3.CO;2

Silitonga PH, Pudjowalujo H, Mollat H (1981) Geological reconnaissance and mineral prospecting on Bacan Island (Moluccas, Indonesia). In: Barber AJ, Wiryosujono S (eds) The geology and tectonics of Eastern Indonesia. Geological Research and Development Centre, Bandung, Special Publication, vol 2, p.373–382

Spell TL, McDougall I (2003) Characterization and calibration of $^{40}Ar/^{39}Ar$ dating standards. Chem Geol 198:189–211. https://doi.org/10.1016/S0009-2541(03)00005-6

Silver EA, Moore JC (1978) The Molucca Sea collision zone, Indonesia. J Geophys Res 83:1681–1691. https://doi.org/10.1029/JB083iB04p01681

Spencer JE (2011) Gently dipping normal faults identified with Space Shuttle radar topography data in central Sulawesi, Indonesia, and some implications for fault mechanics. Earth Planet Sci Lett 308:267–276. https://doi.org/10.1016/j.epsl.2011.06.028

Steiger R, Jager E (1977) Subcommission on geochronology convention on the use of decay constants in geo- and cosmochronology. Earth Planet Sci Lett 36:359–362. https://doi.org/10.1016/0012-821X(77)90060-7

Tera F, Wasserburg GJ (1972) U-Th-Pb systematics in three Apollo 14 basalts and the problem of initial Pb in lunar rocks. Earth Planet Sci Lett 14:281–304. https://doi.org/10.1016/0012-821X(72)90128-8

Tesauro M, Audet P, Kaban MK, Cloetingh S (2012) The effective elastic thickness of the continental lithosphere: Comparison between rheological and inverse approaches. Geochem Geophys Geosyst 13(9):Q09001. https://doi.org/10.1029/2012GC004162

Turcotte DL, Schubert G (2002) Geodynamics, 2nd edn. Cambridge University Press, p xv+56. https://doi.org/10.1017/S0016756802217239

Valley JW (2003) Oxygen Isotopes in Zircon. Rev Mineral Geochem 53:343–385. https://doi.org/10.2113/0530343

Vanderhaeghe O, Teyssier C, McDougall I, Dunlap WJ (2003) Cooling and exhumation of the Shuswap Metamorphic Core Complex constrained by $^{40}Ar/^{39}Ar$ thermochronology. Geol Soc Am Bull 115:200–216. https://doi.org/10.1130/0016-7606(2003)115%3c0200:CAEOTS%3e2.0.CO;2

van Leeuwen TM, Muhardjo, (2005) Stratigraphy and tectonic setting of the Cretaceous and Paleogene volcanic-sedimentary successions in northwest Sulawesi, Indonesia: implications for the Cenozoic evolution of Western and Northern Sulawesi. J Asian Earth Sci 25:481–511. https://doi.org/10.1016/j.jseaes.2004.05.004

van Leeuwen T, Allen CM, Kadarusman A, Elburg M, Palin JM (2007) Petrologic, isotopic, and radiometric age constraints on the origin and tectonic history of the Malino Metamorphic Complex, NW Sulawesi, Indonesia. J Asian Earth Sci 29:751–777. https://doi.org/10.1016/j.jseaes.2006.05.002

van Leeuwen T, Allen CM, Elburg M, Massonne HJ, Palin JM, Hennig J (2016) The Palu Metamorphic Complex, NW Sulawesi, Indonesia: origin and evolution of a young metamorphic terrane with links to Gondwana and Sundaland. J Asian Earth Sci 115:133–152. https://doi.org/10.1016/j.jseaes.2015.09.025

Wallner H, Schmeling H (2011) Sensitivity analysis of rift induced delamination with application to Rwenzori Mountains. Geophys J Int 187:1135–1145. https://doi.org/10.1111/j.1365-246X.2011.05237.x

Watkinson IM, Hall R, Ferdian F (2011) Tectonic re-interpretation of the Banggai-Sula–Molucca Sea margin, Indonesia. In: Hall R, Cottam MA, Wilson MEJ (eds) The SE Asian gateway: history and tectonics of Australia-Asia collision. Geological Society of London Special Publication 355:203–224. https://doi.org/10.1144/SP355.10.

Webb M, White LT (2016) Age and nature of Triassic magmatism in the Netoni Intrusive Complex, West Papua, Indonesia. J Asian Earth Sci 132:58–74. https://doi.org/10.1016/j.jseaes.2016.09.019

Wetherill GW (1956) Discordant uranium-lead ages. Trans Am Geophys Union 37:320–326

White LT, Hall R, Gunawan I, Kohn B (2019) Tectonic mode switches recorded at the northern edge of the Australian Plate during the Pliocene and Pleistocene. Tectonics 38:281–306. https://doi.org/10.1029/2018TC005177

Whitney DL, Teyssier C, Rey P, Buck WR (2013) Continental and oceanic core complexes. Geol Soc Am Bull 125:273–298. https://doi.org/10.1130/b30754.1

Wolf RA, Farley KA, Silver LT (1996) Helium diffusion and low temperature thermochronometry of apatite. Geochim Cosmochim Acta 60:4231–4240. https://doi.org/10.1016/S0016-7037(96)00192-5

Williams IS (1997) U–Th–Pb geochronology by ion microprobe. In: McKibben MA, Shanks III WC and Ridley WI (eds) Applications of microanalytical techniques to understanding mineralizing processes. Reviews in Economic Geology, vol 7, pp 1–35. https://doi.org/10.5382/Rev.07.01

Xu G, Chen Z (2021) Spatial variations of effective elastic thickness of the lithosphere in the Okinawa Trough. J Asian Earth Sci 209:104670. https://doi.org/10.1016/j.jseaes.2021.104670

Yakymchuk C, Kirkland CL, Clark C (2018) Th/U ratios in metamorphic zircon. J Metamorph Geol 36:715–737. https://doi.org/10.1111/jmg.12307

Yasin A (1980) Geologic Map of the Bacan Quadrangle, North Maluku. Geological Research and Development Centre, Bandung

Zandt G, Gilbert H, Owens TJ, Ducea M, Saleeby J, Jones CH (2004) Active foundering of a continental arc root beneath the southern Sierra Nevada in California. Nature 431:41–46. https://doi.org/10.1038/nature02847

Zimmermann S, Hall R (2016) Provenance of Triassic and Jurassic sandstones in the Banda Arc: petrography, heavy minerals and zircon geochronology. Gondwana Res 37:1–19. https://doi.org/10.1016/j.gr.2018.09.008